MESSENGER Neutron Spectrometer Dataset: Tutorial Description of Analysis and Modeling Tasks

Prepared by David J. Lawrence
Johns Hopkins University Applied Physics Laboratory

Table of Contents

Table of Contents ... **i**
Acronyms ... **ii**
1. Introduction ... **1**
2. Summary of MESSENGER NS Data Products ... **2**
3. Reduction of Raw Data to Neutron Count Rates ... **4**
3.1 BP Count Rates: Epithermal and Fast Neutrons ... **4**
4. Description and Validation of Neutron Count Rate Simulation ... **10**
4.1. Simulation Description ... **10**
4.1.1 Calculation of Mercury's surface neutron flux ... 11
4.1.2 Calculation of Area-Efficiency Response ... 12
4.2. Calibration of Simulated Count Rates to Measured Count Rates ... **16**
4.3. Validation of Neutron Simulation ... **18**
4.3.1. Anisotropic Neutron Emission and Detection ... 18
4.3.2. Radial Doppler Effect ... 22
4.3.3. Validation of Neutron Simulation: Summary ... 26
5. Correction of Simulated and Measured Data ... **27**
5.1. Principle of Analysis ... **27**
5.2. Summary of Corrections and Selections ... **28**
5.3. Simulation-only Corrections ... **28**
5.4. Data Selections ... **29**
5.5. Common Simulation/Measurement Corrections ... **31**
5.5.1 Solid Angle Corrections: Epithermal Neutrons ... 31
5.5.2 Spacecraft Obscuration Corrections: Epithermal Neutrons ... 33
5.5.3. Solid Angle and Spacecraft Obscuration Corrections for Fast Neutrons ... 34
5.5.4. Vertical Doppler Correction ... 36
5.6. Corrections Only to Measurements ... **37**
5.6.1. BP Sensor Gain and Background Counts ... 37
5.6.2. NS Dead Time ... 37
5.6.3 Galactic Cosmic Ray Variations ... 37
5.6.4. Energetic Electron (EE) Event Variations ... 38
References: ... **42**

Acronyms

ACS	Anticoincidence Shield
ASCII	American Standard Code for Information Interchange
AU	Astronomical Unit
BP	Borated Plastic
CAD	Calibration And Diagnostic
CMD	Command Echo
CDR	Calibrated Data Record
DDR	Derived Data Record
EDR	Experiment Data Record
EE	Energetic Electron
EVT	Events
FSP	Full Science Package
GAB	Gamma Burst
GCR	Galactic Cosmic Rays
GRaND	Gamma-Ray and Neutron Detector
GRS	Gamma-Ray Spectrometer
HV	High Voltage
LG	Lithium Glass
LG1/2	Inboard(1)/outboard(2) facing LG sensors
MCNPX	Monte Carlo N-Particle eXtended
NCP	Neutron Composition Product
NCR	Net Neutron Count Rate
NS	Neutron Spectrometer
OCM	Orbit-Correction Maneuver
PDS	Planetary Data System
PMT	Photomultiplier Tube
SEP	Solar Energetic Particle
SIS	Software Interface Specification
STA	Status
TTSP	Time To Second Peak
XRS	X-Ray Spectrometer

MESSENGER Neutron Spectrometer Dataset: Description of Analysis and Modeling Tasks

David J. Lawrence
Johns Hopkins University Applied Physics Laboratory

1. Introduction

The Neutron Spectrometer (NS) on NASA's MErcury Surface, Space ENvironment, GEochemistry, and Ranging (MESSENGER) mission was used to measure the elemental composition of Mercury's surface using the technique of planetary neutron spectroscopy. The NS consisted of three scintillator sensors – two Li-glass (LG) sensors and one borated plastic sensor – each read out by a photomultiplier tube (PMT). The two LG sensors are known as LG1 and LG2. The LG1 sensor faces inboard towards the spacecraft, and the LG2 sensor faces outboard (Figure 1). In addition to the NS, the anticoincidence shield (ACS) of MESSENGER's Gamma-Ray Spectrometer (GRS) also measured neutrons from Mercury's surface. Collectively, these sensors measured neutrons with different energies (E_n), ranging from thermal (E_n<0.4 eV), epithermal (0.4<E_n <100 keV), and fast (E_n>500 keV) neutrons. A full description of the NS is beyond the scope of this document, but is provided by *Goldsten et al.* [2007].

Data from the NS (and ACS) have been used to measure the composition and distribution of neutron absorbing elements on Mercury's surface [*Lawrence et al.*, 2010, *Peplowski et al.*, 2015], variations in fast neutrons, which are related to average atomic mass [*Lawrence et al.*, 2016a], regional carbon concentrations [*Peplowski et al.*, 2016], and hydrogen concentrations at Mercury's North Pole [*Lawrence et al.*, 2013]. In addition to composition measurements, data from the NS have been used to carry out studies in solar physics [*Feldman et al.*, 2010, 2015, *Lawrence et al.*, 2014, 2015b], cosmic-ray physics [*Rodgers et al.*, 2015, *Lawrence et al.*, 2016b], and Mercury magnetospheric physics [*Ho et al.*, 2011, *Lawrence et al.*, 2015a]. To fully utilize the NS dataset for these different studies, multiple analysis and modeling tasks were carried out. However, the description of these tasks is spread out in multiple peer-reviewed publications and PDS documents. To facilitate a better use of the NS data, this document combines a description of these analysis and modeling tasks in one location. In some cases, these descriptions are taken directly from the prior publications. In other cases, updates are made to the prior descriptions. Where needed and appropriate, new descriptions and figures are provided in this document that do not appear elsewhere.

To provide a proper attribution of where information in this document has appeared elsewhere (sometimes in modified form), Table 1 provides a list of all publications that this document draws from, including the specific sections linked to prior publications.

Publication	**Figure and Sections In this Document**
Lawrence et al. [2010], "Identification and measurement of neutron-absorbing elements on Mercury's surface"	Section 4.1; Fig. 1, Fig. 8
Lawrence et al. [2013], Supplemental Material of "Evidence for water ice near Mercury's north pole from MESSENGER Neutron Spectrometer measurements"	Sections 3.1, 4.1, 4.2, Section 5; Figs. 2 – 5, Figs. 10 – 20, Figs. 23 – 25.
[*Lawrence et al.*, 2016a], "Compositional Terranes on Mercury: Information from Fast Neutrons"	Section 5.5.3; Figs. 21 – 22.
Lawrence et al. [2016b], "Galactic cosmic ray variations in the inner heliosphere from solar distances less than 0.5AU: Measurements from the MESSENGER Neutron Spectrometer"	Table 1
New to this document	Sections 1 and 2; Figs. 7, 9; Table 2

Table 1. List of papers that contain information (text and figures; sometime modified) given in this document. Right column lists the sections that contain the information from the given paper.

2. Summary of MESSENGER NS Data Products

All MESSENGER NS data products are available from the NASA Planetary Data System (PDS) on the web page: http://pds-geosciences/wustl.edu/missions/messenger/grns.htm. The MESSENGER NS dataset contains three types of data products, which are Experiment Data Records (EDR), Calibrated Data Records (CDR), and Derived Data Records (DDR). Details of each of these datasets are described in two associated Software Interface Specification (SIS) documents. The EDR dataset is described in the NS EDR SIS ("nsedrsis.pdf" file found on the above web page); the

CDR and DDR datasets are described in the NS CDR-DDR SIS ("ns_cdr_ddr_sis.pdf" file found on the above web page).

The EDR dataset contains 10 separate file types, which are: Full Science Spectra (FSP), Spectra, Events (EVT), Galactic Cosmic Ray (GCR), GAmma Burst (GAB), Short Science, Time-Correlated Counts, Status (STA), Calibration and Diagnostic (CAD), and Command Echo (CMD). Of these file types, three were effectively discontinued prior to Mercury orbit insertion: Spectra, Short Science, and Time-Correlated Counts. The remaining seven file types – FSP, EVT, GCR, GAB, STA, CAD, CMD – compromised the large majority of the NS cruise and orbital EDR data. The NS EDR data contain one file per day per file type, with a binary data format that is described in the NS EDR SIS.

The CDR dataset contains five file types, which are: NS Spectra, NS Counts, NS Galactic Cosmic Ray Spectra, NS Engineering Data, and NS Gamma-Ray Burst data. In these files, the EDR data have minor processing steps applied, and except for the Gamma-Ray Burst data, are merged with MESSENGER spacecraft ephemeris data. The CDR data are the primary data used and described in this document, and are the "Raw" data discussed in Section 3. The processing steps to go from the EDR to CDR data are described in a filed called the "MESSENGER Neutron Spectrometer (NS) EDR-to-CDR-to-DDR Processing" document ("messns_processing.pdf" file on the MESSENGER NS PDS web page). The NS CDR data contain one file per day per file type, and are stored in a binary data format that is described in the NS CDR-DDR SIS document.

The DDR dataset contains two file types, which are Net Neutron Count Rates (NCR) and a Neutron Composition Product (NCP). The NCR files are a Level 2-type data product where the data reduction steps described in Section 3 are applied. A summarized description of these data reduction steps is also provided in the "messns_processing.pdf" document. These files contain one file per day of net neutron count rates from each of the NS sensors along with all the MESSENGER spacecraft ephemeris data that are contained in the CDR data. These data are stored in an ASCII data format that is described in the NS CDR-DDR SIS document. The NCP data contain ASCII column data of relative neutron count rates for the latitude bands as presented in *Lawrence et al.* [2013] The "messns_processing.pdf" document provide additional details of the data analysis and processing that was carried out to create the CDR and DDR datasets, and is a complementary document to this document.

3. Reduction of Raw Data to Neutron Count Rates

Schematic views of the NS are shown in Figure 1. The NS contained a 10 cm x 10 cm x 10 cm borated plastic (BP) scintillator and two 10 cm x 10 cm x 4 mm Li-glass (LG) scintillators (Figure 1c). Each sensor is read out by a PMT (Figure 1b). The NS was located on the spacecraft deck opposite of the sunshade (Figure 1a), where it had a ~2π unobstructed field of view. The spacecraft +z deck was generally planet facing during low-altitude operations, giving NS a relatively unobstructed view of Mercury.

The NS produces three different types of data; scalars, energy deposition spectra, and time-correlated double-coincidence event-mode data. Scalars report the total event rate in the sensors, including singles rates in each sensor, double coincidence rates between any two detectors, the triple coincidence rate (all three detectors), and the fast neutron rate derived from time-correlated BP counts. Energy deposition spectra from all three sensors are used to derive neutron count rates that are reported in the NS PDS data products. All are recorded as a time series, with associated ephemeris information appended to each daily record on an identical time basis. The double-coincidence event-mode data record individual fast-neutron events in the BP sensor.

The LG-energy-spectrum-derived neutron count rates measure thermal and epithermal neutrons, where the energy discrimination is achieved using Doppler filter spectroscopy [*Feldman and Drake*, 1986]. The BP-energy-spectrum-derived count rates measure epithermal neutrons. The time-correlated BP counts, both the scalar values and the event-mode data, measure fast neutrons. The reduction analyses used to derive BP neutron count rates from BP energy deposition spectra are described in Section 3.1, and the reduction analyses for the LG sensors is described in Section 3.2.

3.1 BP Count Rates: Epithermal and Fast Neutrons

Fast and epithermal neutron count rates were derived from measurements made with the borated plastic (BP) sensor of the MESSENGER NS, which is described by *Goldsten et al.* [2007]. Count rates for fast neutrons ($0.5 < E_n < 10$ MeV) were obtained from a two-

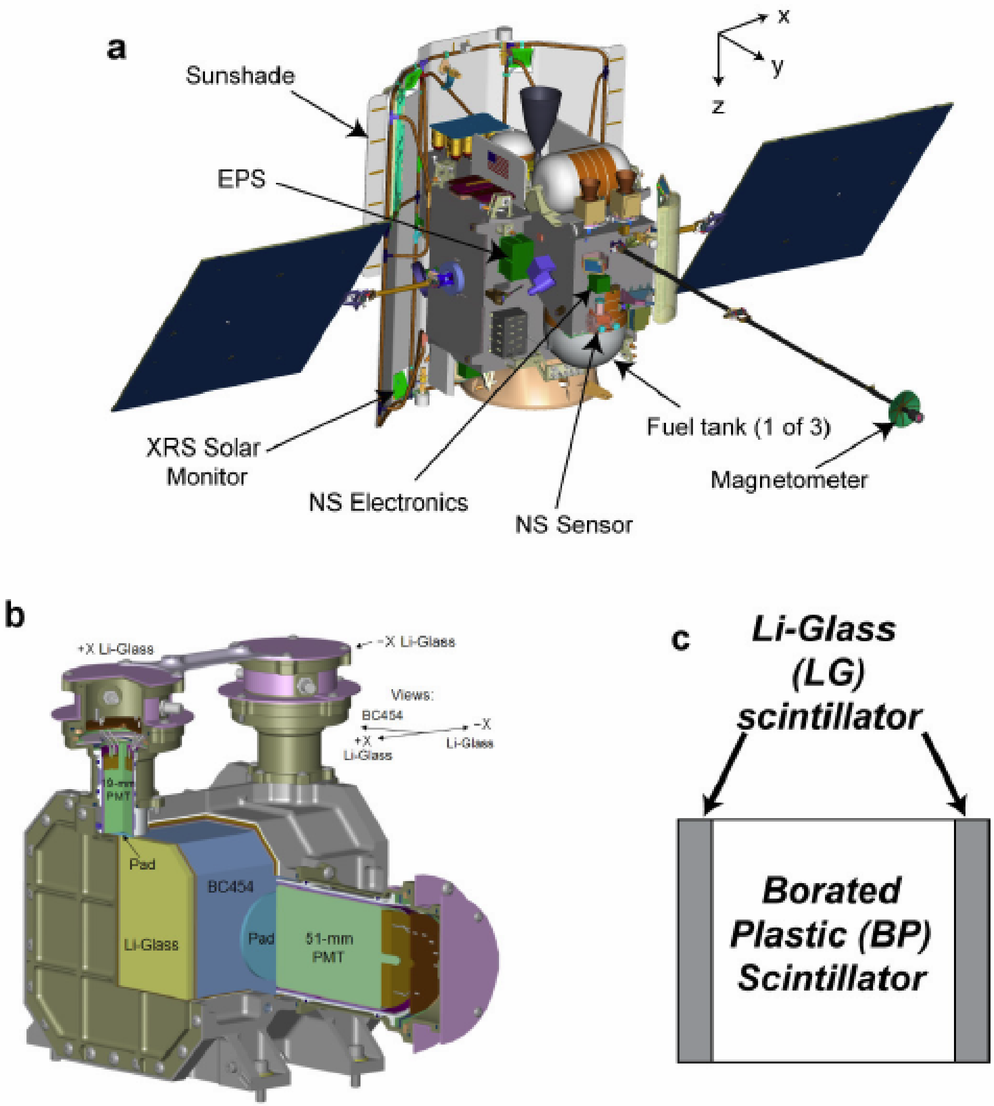

Figure 1. (a) Engineering drawing of the MESSENGER spacecraft [*Leary et al.*, 2007] showing the locations of the Neutron Spectrometer (NS sensor), X-Ray Spectrometer (XRS) solar monitor, Magnetometer, and Energetic Particle Spectrometer (EPS) sensor relative to the sunshade at left and the three intervening fuel tanks that shield the NS from the Sun. (b) Engineering drawing of the MESSENGER NS and a simplified schematic of the placement of the three NS sensor components. BC454 in Figure 1b refers to the designation of (c) the borated plastic scintillator.

pulse sequence in the BP scintillator. With each particle, an initial prompt pulse is caused by the energy loss of recoil protons in the scintillator and provides a measure energy loss in the scintillator with an energy resolution of better than 50%. A second neutron-capture pulse unambiguously identifies a neutron event via its 93 keV electron-equivalent (keV_{ee}) energy from the $^{10}B(n,\alpha)$ reaction along with a 2-μs characteristic

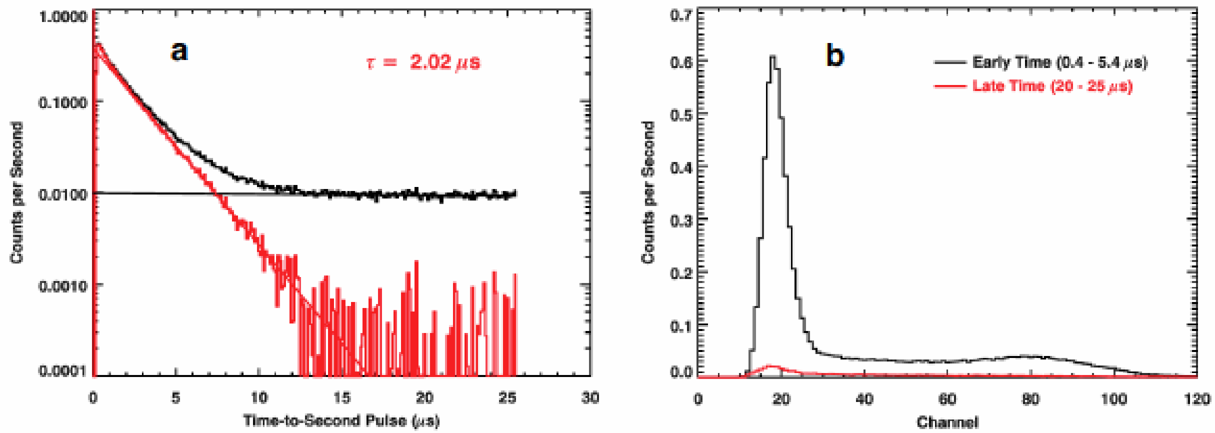

Figure 2. MESSENGER NS fast neutron event data taken from 10 – 15 April 2011 and averaged over periods for which altitudes were lower than 1500 km. (**a**) Histograms of counts per second of the time to second pulse (TTSP) versus TTSP (black) and the late-time-subtracted portion of the TTSP (red); the straight red line indicates an exponential fit for a decay time τ of 2.02 μs. (**b**) Histograms of second pulses for early times (black) and late times (red).

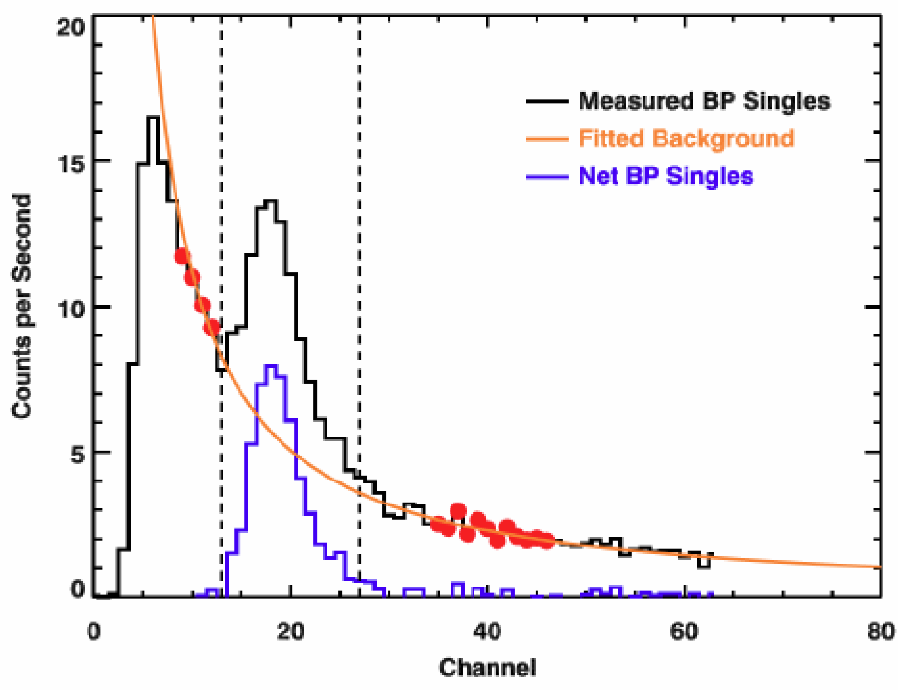

Figure 3. Pulse height spectra of single-event interactions (singles) from the MESSENGER NS borated plastic (BP) sensor taken from a single 20-s accumulation period on 10 April 2011 (3:58:43 UTC) when the MESSENGER spacecraft was at an altitude of 702 km. Gain-corrected spectra are shown in black. A power law shown as an orange trace was fit to the background data points shown as red circles. The net spectrum is shown in blue. Channel limits for summed, net count rate are shown as vertical dashed lines.

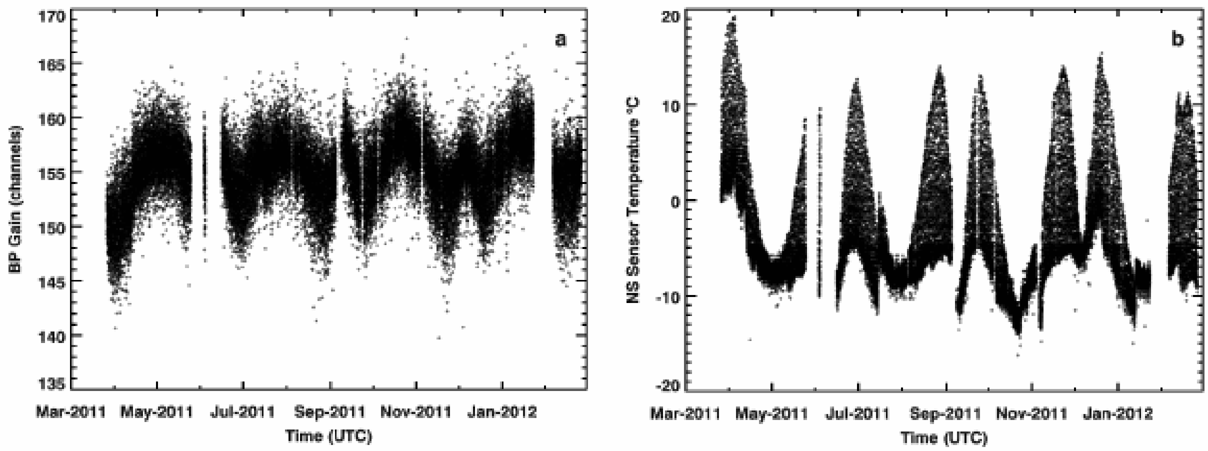

Figure 4. **(a)** Gain of the BP sensor measured using the peak position from the second-event fast neutron data on 15-min increments (channel numbers are higher than in Fig. S1B as this measurement used a higher bit resolution for the pulse height data). Gain data are shown from 26 March 2011 to 25 February 2012. **(b)** NS sensor temperature values for the same 15-min time increments as for the gain values.

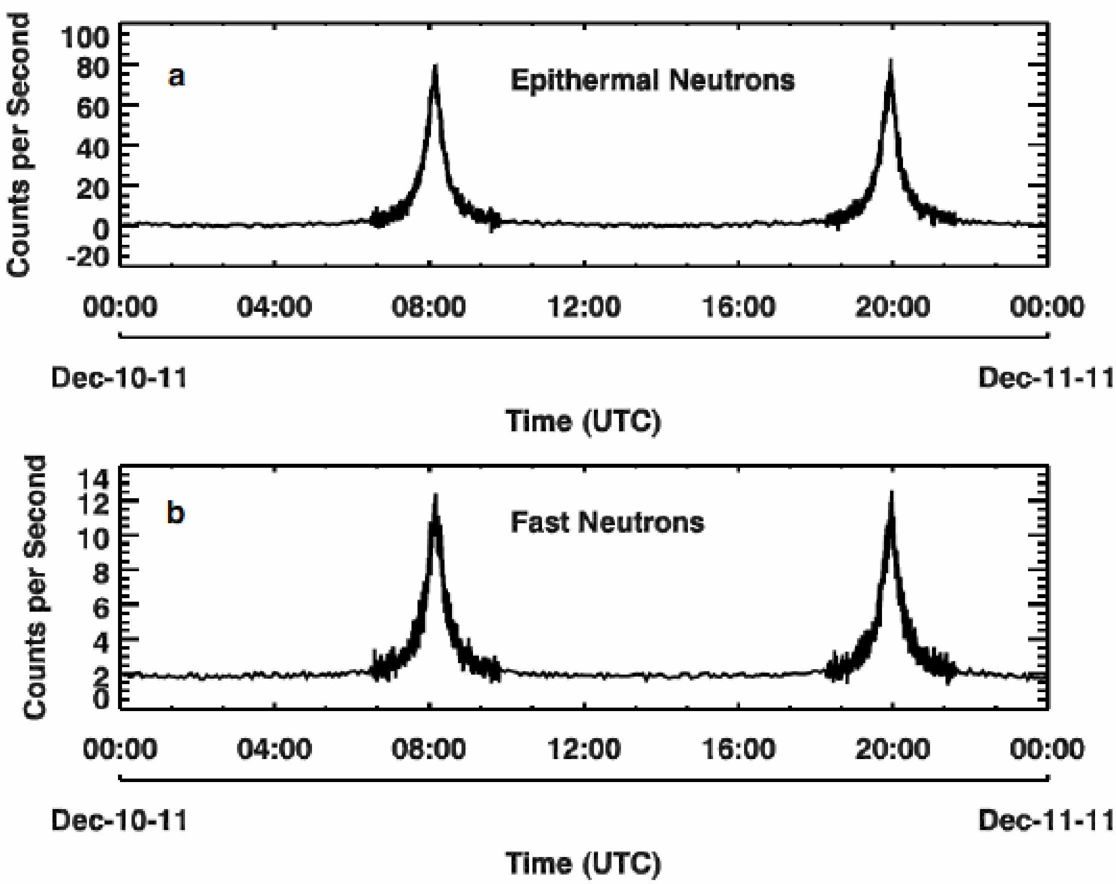

Figure 5. Net (**a**) epithermal and (**b**) fast neutron count rates for a single Earth day in Mercury orbit.

mean time delay from the prompt pulse [*Goldsten et al.*, 2007]. Figure 2 shows histograms of time to second pulse (TTSP) and second pulse data collected in orbit using the event-mode data about Mercury and demonstrates the capability of the NS for fast neutron identification. The net fast neutrons are the counts detected for early TTSP values less the background of late TTSP values, following a methodology that was applied earlier to fast neutron measurements at other planetary bodies [e.g., *Feldman et al.*, 2004].

The epithermal neutron count rate was obtained from the BP pulse-height histogram for single-event interactions (singles). Figure 3 shows a BP singles pulse-height histogram for a single 20-s data accumulation period. When close to the planet, the measured spectrum has two components: a 93 keV_{ee} peak due to the $^{10}B(n,\alpha)$ reaction of neutrons captured in the scintillator, and background counts due to various charged particles and high-energy photons that deposit energy in the BP sensor. Throughout the orbital mission, sensor temperature variations cause the gain of the BP sensor and electronics to change by 12–13%. To ensure that the BP spectral components stay at the same equivalent-electron energy channels, the BP gain was measured in 15-min intervals using the $^{10}B(n,\alpha)$ peak channel position from the fast neutron second pulse (Figure 2b). Figure 4 shows both the measured gain variation and the inversely varying NS sensor temperature. With this measured gain, the BP spectra were gain shifted to standardized channels using the procedure described by *Lawrence et al.* [2004].

Following procedures used for similar neutron spectrometers on the Mars Odyssey and Dawn spacecraft [*Maurice et al.*, 2004, *Prettyman et al.*, 2011], count rates for channels below and above the neutron peak were fit with a power law to empirically determine the shape of the background continuum. This fit of the continuum was subtracted from the original spectrum to obtain a net BP spectrum. The net epithermal neutron counts were defined as the summed counts within a channel window around the neutron peak (vertical dashed lines in Figure 3). This process was repeated on a spectrum-by-spectrum basis, and the counts within the peak were divided by the livetime-corrected accumulation time to produce the time-series neutron count rates as measured by the BP sensor.

Example epithermal and fast neutron counting rates for one Earth day of NS data are shown in Figure 5. For each Earth day during the primary mission, the MESSENGER spacecraft had two periapsis passes around Mercury during its 12-h orbit. As the spacecraft approached the planet, there was a corresponding increase in the neutron count rate (at 08:00 and 20:00 UTC in Figure 5). The NS has two different data accumulation periods. When the spacecraft is within 6000 km altitude, the NS collects data with 20-s accumulation periods. At higher altitudes, the data collection cadence is 300 s. The larger scatter seen in the near-planet data is due to the fact that these data were collected over the shorter 20-s time period. The high-altitude count rates of nearly 0 counts per second (cps) for epithermal neutrons and 2 cps for fast neutrons are consistent with those measured during pre-orbit cruise periods.

3.2 LG Count Rates: Thermal and Epithermal Neutrons

The algorithm used to derive the net neutron counts for the LG sensors is illustrated in Figure 6. A representative, 20-s integration energy deposition spectrum from each LG sensor is shown in Figure 6 as the solid black line. To isolate the neutron capture peak (ch ~30), an empirical background function is subtracted from the main spectra. This background function (dotted, black line) was derived from the averaged, high-altitude spectra for each given day, where high-altitude is defined to include spectra collected when the spacecraft was above 8000 km. A background-subtracted spectrum is calculated for each time step as the difference between the original spectrum and the average background spectrum. The background-subtracted spectrum is fit to a Gaussian plus second-order polynomial function to determine both the peak and remaining background counts. Of the three Gaussian parameters (peak position, peak width, peak height), only the peak height is allowed to vary as the other parameters are constrained by gain-corrected values that are empirically determined using data accumulated over long periods of time. This procedure therefore assumes that the gain-corrected peak parameters remain constant and only the peak height varies. The three parameters of the polynomial portion of the fitting function are allowed to vary. The net neutron count rate is the area under the Gaussian portion of the fitting function. The uncertainties in the net neutron count rates are the calculated uncertainties due to the fitting procedure. Peak

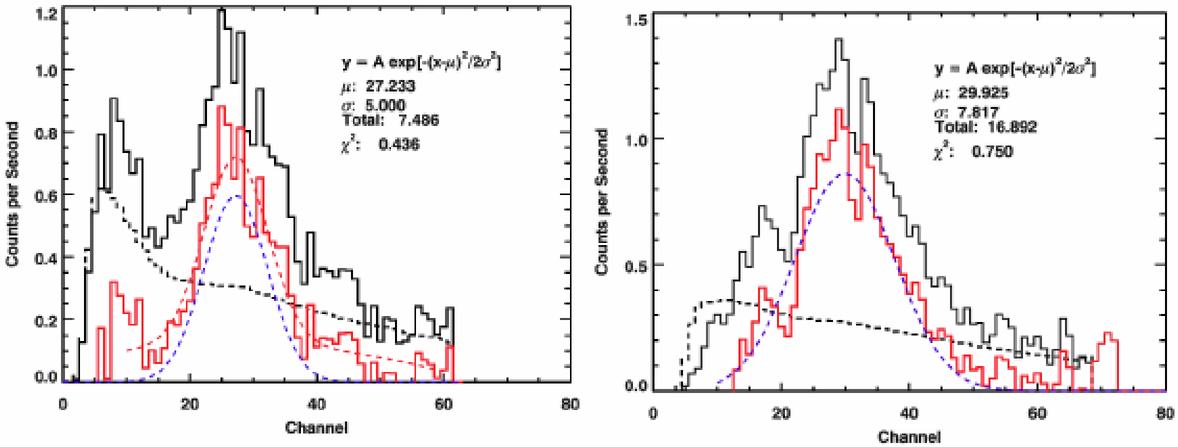

Figure 6. Pulse height data from a single 20-second time collection from the LG1 (left) and LG2 (right) sensors. The black, solid line shows the original, gain corrected data. The dotted black line shows the high-altitude background spectra. The solid red line shows the background-subtracted spectra. The dotted, red line shows the fit of a Gaussian plus polynomial function to the background-subtracted spectra. The dotted, blue line shows the Gaussian portion of the fitted spectra.

areas derived from this technique are divided by the live time corrected accumulation time and reported as a neutron count rate time series in the NS PDS products.

4. Description and Validation of Neutron Count Rate Simulation

4.1. Simulation Description

To understand the effects of Doppler thermal-neutron enhancement and spacecraft obscuration and attenuation, and more generally how the NS data are related to Mercury's surface composition, the neutron transport from Mercury's surface to the NS must be modeled. Specifically, the neutron transport properties of the spacecraft materials need to be explicitly taken into account. *Feldman et al.* [1989] gave a generalized expression for the neutron counting rate, C, measured from a spacecraft moving around a planet:

$$C = \frac{N}{2\pi}\int d\varphi \int d\mu \int dK \frac{\mathbf{V}_T \cdot \hat{n}}{|\mathbf{V}|} A\,\varepsilon(\varphi_D,\mu_D,K_D)\Phi(\varphi,\mu,K) \qquad (1)$$

The integral is calculated over angular variables φ and $\mu = \cos(\theta)$ from within a spacecraft nadir-fixed coordinate system (where φ is the azimuth angle and θ is the polar angle relative to the nadir direction) and energy K. The GCR-induced neutron flux at orbital altitude, Φ (assumed to be azimuthally symmetric), is modeled for a variety of surface compositions and is calculated in terms of neutrons per incident GCR proton per cm^2. An overall normalization factor, N, includes factors to account for the absolute GCR flux. The area-efficiency response of the NS, which includes the neutron response of the spacecraft, is given by $A\varepsilon$, where A is the detector area and ε is the detector efficiency. ε is dependent on spacecraft-fixed angles and energies (φ_D, μ_D, K_D), which themselves are dependent on the spacecraft nadir-fixed angles and energies. Equation (1) includes a velocity dot-product term, where $\hat{n}$ is the unit vector normal to the sensor being modeled, $\mathbf{V}_T$ is the velocity of the neutron in the frame of the detector, and $\mathbf{V}$ is the velocity of the neutron at the altitude of detection. A summary of how the two main terms in equation (1) are calculated – surface neutron flux and NS area-efficiency response – is given below.

4.1.1 Calculation of Mercury's surface neutron flux

The surface neutron flux from Mercury was calculated in a manner similar to previous calculations for lunar soils [*McKinney et al.*, 2006, *Lawrence et al.*, 2006]. We used the Monte Carlo particle transport code MCNPX [*Pelowitz*, 2005] and provided an initial GCR proton flux to model the neutron production, transport, and absorption from a spherical Mercury surface. The effects of gravity and finite neutron lifetime were explicitly taken into account within the MCNPX calculations that derive the neutron flux at the surface of Mercury. For a GCR energy-dependent flux spectrum, we used the parameterization for protons and alpha particles given by *Masarik and Reedy* [1996] that depends on a solar modulation parameter, ϕ, which affects both the shape and absolute normalization of the spectrum. To obtain the solar modulation parameter, we used the procedure of *McKinney et al.* [2006] and Earth-based South-Pole neutron monitor data to estimate that ϕ for various time periods. For the Mercury flyby data of the M1 flyby [*Lawrence et al.*, 2010], we used ϕ = 300 MV. For other analyses [e.g., *Lawrence et al.*, 2013, *Lawrence et al.*, 2016a], a value of ϕ = 550 MV was used. The Mercury neutron fluxes were calculated for a variety of temperatures and Mercury soil compositions. Exact values are given in the respective studies [*Lawrence et al.*, 2010, 2013, 2016a, *Peplowski et al.*, 2015, 2016]. As a final step, the modeled surface neutron fluxes were analytically transformed to neutron fluxes at orbital altitude using the relations given by *Feldman et al.* [1989] that account for the curved neutron ballistic trajectories, gravitational binding, and finite lifetime of thermal neutrons.

4.1.2 Calculation of Area-Efficiency Response

The area-efficiency response of the NS-spacecraft combination was calculated using MCNPX. The NS and spacecraft were modeled with 166 cells, each of which represents a portion of a spacecraft part and/or subassembly (Figure 7). The most detailed part of this model was the NS, where the sensors, PMTs, Mg housing, and Gd shielding were explicitly modeled. For the spacecraft, we modeled the major components expected to affect the neutron transport through the spacecraft. These include the five spacecraft fuel tanks (both the tank material and fuel), the phased-array antenna located close to the NS, the sunshade, the main spacecraft battery, the main thrusters, the carbon composite

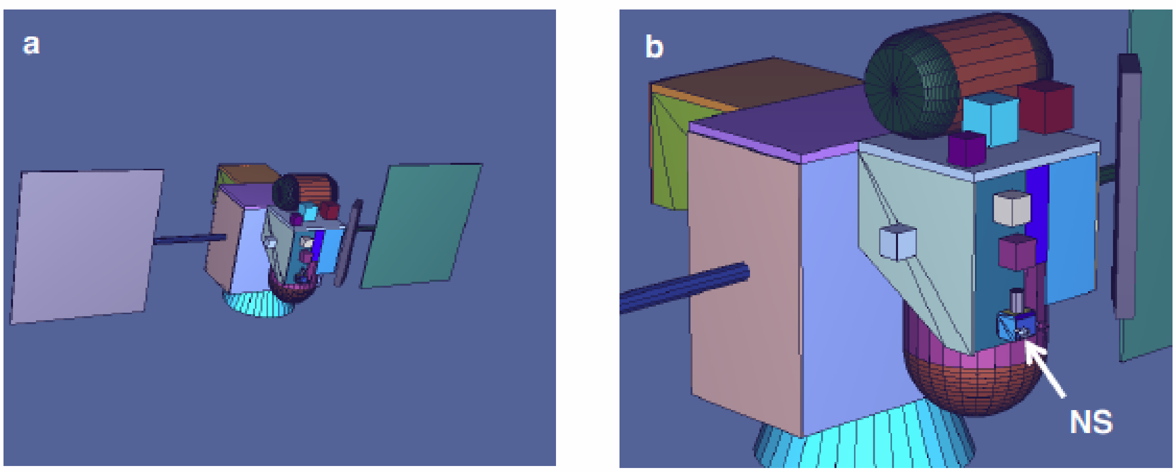

Figure 7. MCNPX geometry model of the MESSENGER spacecraft model for the NS-spacecraft area-efficiency response calculations. (**a**) Full spacecraft model. (**b**) Focused view on the central portion of the spacecraft. The NS is highlighted with an arrow.

spacecraft structure, and a variety of instruments and electronics located around the spacecraft. For all electronics and sensor boxes, we used a standard electronics board composition and calculated a density that matched the volume-mass combination for each box. For some parts or groups of parts that were difficult to model in great detail (e.g., cable harnesses, fuel plumbing systems), we distributed the mass of the parts in the general vicinity of where the parts were located. For each of the flybys and orbital portions of the mission, we used a fuel loading appropriate to each, with a 65%, 61%, and 50% fuel loading for first, second, and third Mercury flybys, respectively; for modeling of orbital data, a fuel loading of ~13% was used. The fuel composition was hydrazine (N_2H_4) and nitrogen tetroxide (N_2O_4)[*Leary et al.*, 2007]. Due to the close proximity of the carbon composite structure to the NS, uncertainties in the construction of this structure will have the largest effect in the modeled NS response. We therefore attempted to model this structure with as much precision as possible. We explicitly accounted for 15 mils of Cu grounding [*Leary et al.*, 2007] on the structure [Cu has a large thermal neutron absorption cross section of 4.47 barns (b)]. The carbon composite structure consists of two faceplates covering an irregular ribbed structure. Because the ribbed structure is too fine and variable in scale across the spacecraft to model explicitly, a combination of spacecraft drawings and empirical pre-launch measurements was used to determine that the carbon composite density was 0.32±0.03 g/cm^3. The composition of the carbon composite structure is 70% carbon (fiber) plus 30% cyanate ester epoxy resin. In summary, our modeled spacecraft dry mass is 504 kg, which is within less than 1% of the final spacecraft dry mass of 508 kg [*Leary et al.*, 2007]. Calculations made with spacecraft models having somewhat different total dry mass indicate that such a small difference in mass has a negligible effect on the overall NS response.

To obtain the area-efficiency response of the sensors, the entire spacecraft was illuminated with plane-wave (mono-directional) neutrons having 31 different energies ranging from 10^{-9} to 10 MeV) and 104 different azimuth and elevation angle combinations. For each neutron energy, the modeled angular response was interpolated over a sphere to create the final response function grid on 5º x 5º grid points. Figure 8 shows maps of the LG response for three different neutron energies. For low-energy neutrons (0.0066 eV) in which the intrinsic efficiency of the LG scintillators is near 100%, the modeled effective area is close to 100 cm^2, which is the physical area of each scintillator. For LG1, the effect of the phased-array antenna that lies within the LG1 field of view is seen around 10º horizontal, 45º vertical. For medium-energy neutrons (10 keV), the response is smoother and more diffuse because the higher-energy neutrons are more penetrating and not as attenuated by the spacecraft material. Finally, for high-

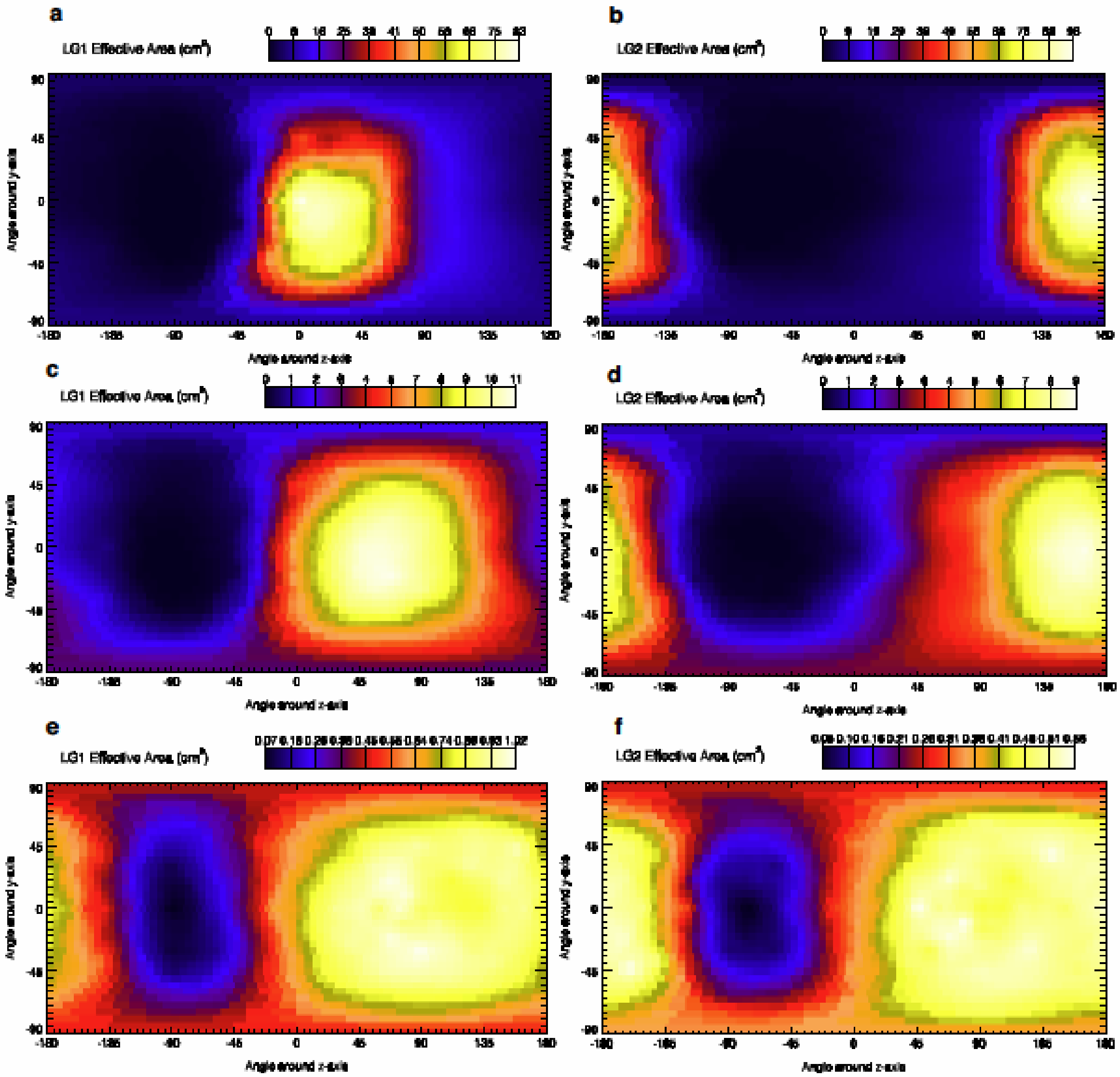

Figure 8. Maps of the LG response in units of effective area (cm^2). The center of the map is the response for an incoming direction corresponding to the spacecraft x-axis. Horizontal angles correspond to angles measured anticlockwise around the spacecraft z-axis starting from 0°; vertical angles correspond to angles measured anticlockwise around the spacecraft y-axis starting from 0°. Figures (a), (c), and (e) show the LG1 response and (b), (d), and (f) show the LG2 response. Figures (a) and (b) show the response for low neutron energies (0.0066 eV), (c) and (d) show the response for medium neutron energies (10 keV), and (e) and (f) show the response for high neutron energies (10 MeV).

energy neutrons (10 MeV), there is a general diffuse response, which is likely due to the spacecraft material resulting in less attenuation, as well as the down-scatter of higher-energy neutrons to lower energies where they are more efficiently detected with the LG sensors.

The effective area for the BP epithermal and fast neutron measurements was calculated with the same particle transport code MCNPX as was used for the LG sensors.

For epithermal neutrons, a ^{10}B capture flux tally was the basis for calculating the BP singles epithermal effective area, which is shown in Figure 9 for four different neutron energies.

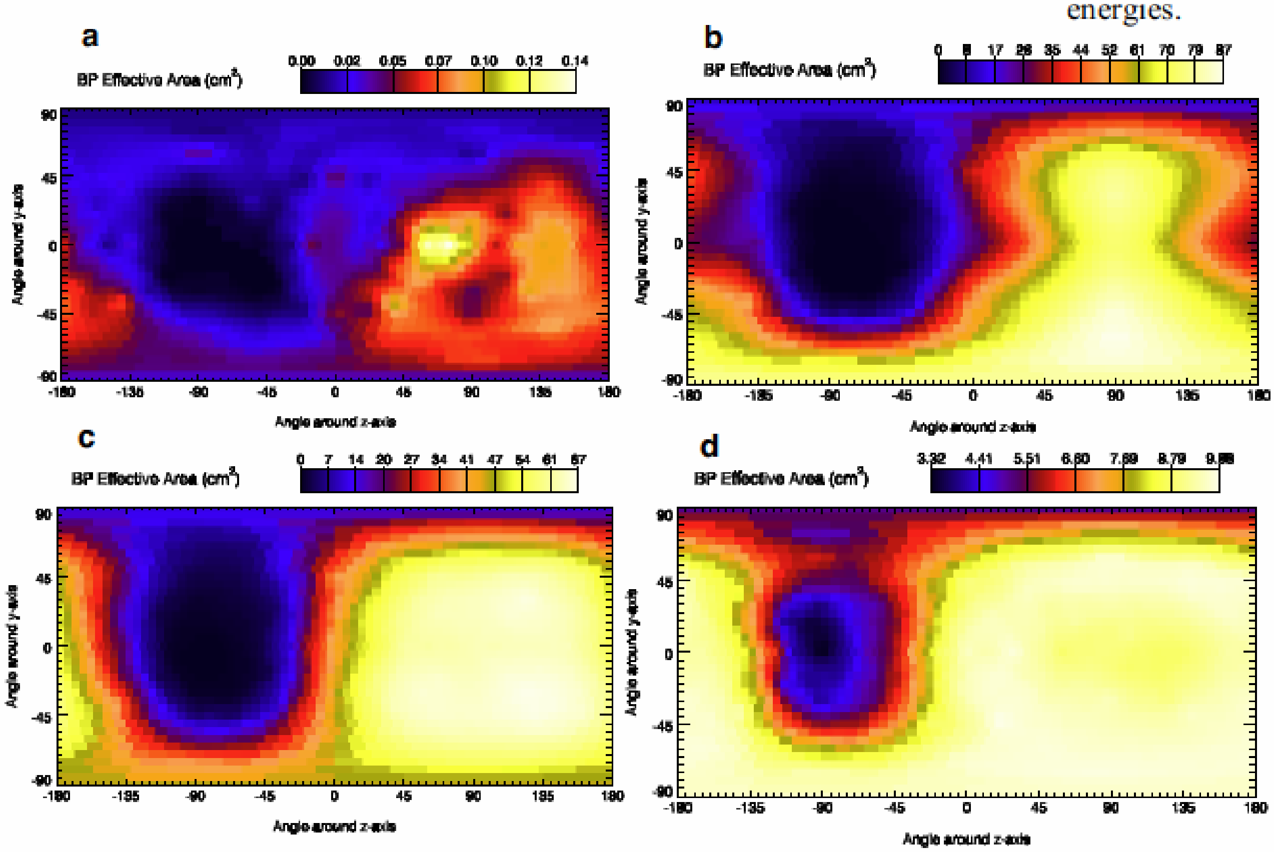

Figure 9. Maps of the BP response in units of effective area (cm^2). The center of the map is the response for an incoming direction corresponding to the spacecraft x-axis. Horizontal angles correspond to angles measured anticlockwise around the spacecraft z-axis starting from 0°; vertical angles correspond to angles measured anticlockwise around the spacecraft y-axis starting from 0°. Figure (a) shows the response for the thermal neutron energies (0.0066 eV), (b) shows the response for low-energy epithermal neutron energies (0.66 eV), (c) shows the response for high-energy epithermal neutron energies (10 keV), and (d) shows the response for high neutron energies (10 MeV).

For fast neutrons, we used a hybrid approach to calculate the effective area. The reason for the hybrid approach is because the standard MCNPX code is not able to calculate the full energy-dependent double-pulse fast neutron efficiency of the BP sensor. For portions of the calculations in which the shape of the fast neutron spectra from Mercury does not change and an energy-dependent efficiency is not needed for neutrons entering the sensor, we used a ^{10}B capture flux tally for energies above 500 keV, which is the approximate fast neutron detection threshold. When the simulated fast neutron count rates were scaled to hydrogen concentration [*Lawrence et al.*, 2013], a full energy-dependent fast neutron efficiency function was used (Figure 10). This function was calculated using a custom version of MCNPX that does account for the BP double pulse interaction. A similar efficiency function was calculated using the same custom MCNPX code for the Dawn Gamma-Ray and Neutron Detector (GRaND) [*Prettyman et al.*, 2011]. In addition to the fast-neutron efficiency, a calibration of the fast-neutron energy scaling was carried out, and is described in detail in Appendix B of *Lawrence et al.* [2014].

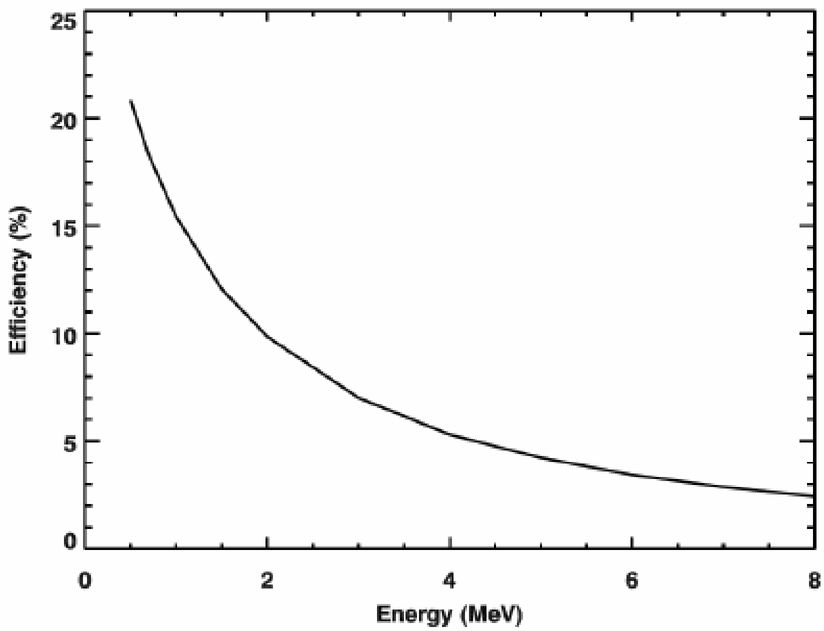

Figure 10. Fast neutron efficiency for the BP sensor calculated using techniques described by *Prettyman et al.* [2011]

4.2. Calibration of Simulated Count Rates to Measured Count Rates

The first step for using and validating the count rate simulation was to directly compare uncorrected measured and simulated count rates. Figure 11 shows simulated versus measured count rates for 10 days of fast and epithermal (BP) neutrons when the spacecraft altitude was less than 4000 km. Each data point indicates a single 20-s accumulation. Figure 11 shows an excellent correlation between the simulated and measured count rates with a correlation coefficient of 0.97 and 0.98 for the fast and epithermal counts, respectively. For this figure, the simulated counts were calculated without Poisson uncertainties included. The scatter in the data is therefore due only to

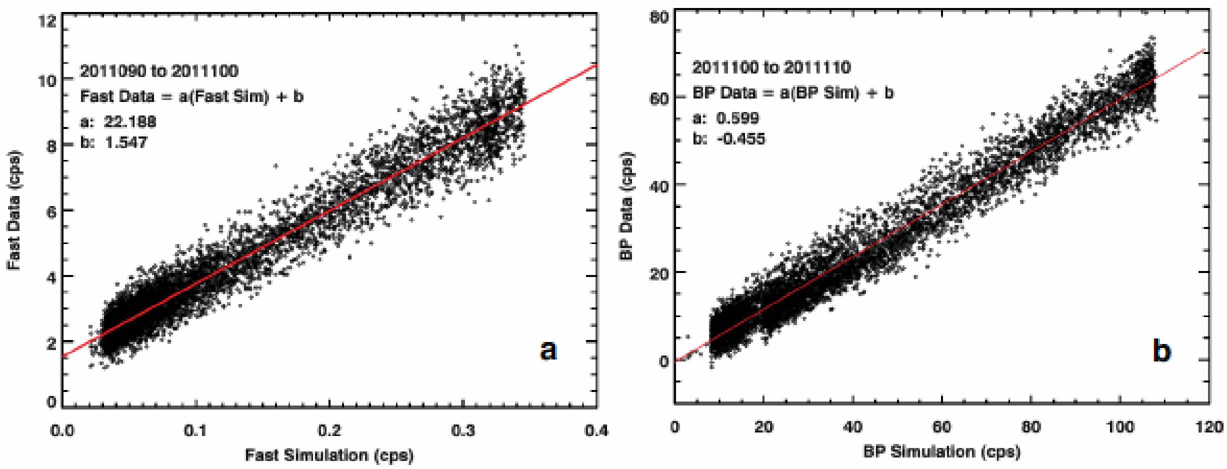

Figure 11. Simulated versus measured (**a**) fast and (**b**) BP neutron data, where BP is a measure of epithermal neutrons. Times are taken from 10 to 20 April 2011 and for altitudes less than 4000 km. The solid red line shows a linear fit to each dataset.

Poisson and other unmodeled variations in the measured data. For example, galactic cosmic ray (GCR) induced variability, which results in variations in Mercury's neutron flux, at are not included in the model, which assumes a time-invariant neutron flux. The excellent correlation between simulated and measured data provides an initial and robust validation of the simulation code for fast and epithermal neutrons. The fitting constants of Figure 11 were used as scaling and offset factors for connecting the simulated to the measured data. Count rates from the LG sensor (not shown) show similar behavior, as do measured and modeled count rates from the GRS ACS [*Peplowski et al.*, 2015].

The relatively large scaling factor for the fast neutrons (22.2) reflects the fact that the absolute efficiency for the fast neutron double-pulse interaction is not fully taken into account in this set of calculations. The offset value of 1.55 cps reflects the background fast neutron measurements on the spacecraft when far from Mercury. The scaling factor for the epithermal neutrons (0.6) is closer to unity than for the fast neutrons; its deviation from unity reflects an imperfect knowledge of various normalization factors (e.g., absolute GCR flux). A negative offset may reflect a slight over-subtraction of the epithermal neutron background function. For all subsequent analyses, the scale values are applied to the simulation data and the offset values are applied to the measured data to ensure a proper calibration of simulated to measured counts.

4.3. Validation of Neutron Simulation

Given that the fast and epithermal neutron count rates need to be understood and corrected to better than 1% accuracy [*Lawrence et al.*, 2011, 2013, 2016a], additional validation of the simulated count rates must be demonstrated to ensure that the simulated count rates are a reliable guide for understanding the measured data. The data correction with the largest magnitude is the correction carried out for variations in solid angle:

$$\Omega(h) = \int_{\cos\theta=\cos\theta_{\max}(h)}^{1} \int_{\varphi=0}^{2\pi} f(\theta,\varphi,h)\, d\cos\theta\, d\varphi, \quad (2)$$

where h is the spacecraft altitude above the surface, θ and φ are the polar and azimuthal angles relative to the sensor-Mercury center vector, $\theta_{\max}(h) = \sin^{-1}[R_M/(R_M+h)]$ is the polar angle of the horizon at an altitude h above a planet with radius R_M, and $f(\theta,\varphi,h)$ is a generic function to account for departures from isotropy for emission and detection. In most orbital mapping scenarios, the departure from isotropy is small, and the function $f(\theta,\varphi,h)$ is set to 1 so that Equation 2 can be analytically integrated to

$$\Omega(h) = 2\pi\left[1-\cos\theta_{\max}(h)\right]. \quad (3)$$

If either the neutron emission or the detection functions are not isotropic, however, or if there are additional altitude dependencies, then $f(\theta,\varphi,h)$ will not be a constant and Equation 3 will not properly represent the full solid-angle variation. In this section, we describe two modifications to the $f = 1$ analytic approximation. The first modification relates to anisotropic emission and detection and applies to both fast and epithermal neutrons. The second modification relates to the radial Doppler effect and applies only to epithermal neutrons.

4.3.1. Anisotropic Neutron Emission and Detection

An anisotropic solid angle dependence can result from anisotropies in both neutron emission and detection. *Maurice et al.* [2004] provided evidence for anisotropic emission using LP-NS epithermal neutron data from the early elliptical-orbit portion of the Lunar Prospector (LP) mission. *Maurice et al.* [2004] modified Equation 3 to include a term that accounts for an angular anisotropy:

$$\frac{\Omega(h)}{2\pi} = 1 - \cos \nu(h), \quad (4)$$

where

$$\nu = \sin^{-1}\left(\frac{R_m}{R_m + h}\sin\eta\right). \quad (5)$$

Here, η is an empirically determined parameter that accounts for the angular anisotropy and takes the value η = 90º for a fully isotropic emission and detection. By fitting LP-NS data to Equation 4, *Maurice et al.* [2004] found η_{LP} = 80º and attributed the departure of η from 90º to an anisotropic neutron emission from the surface. In a separate study, *Lawrence et al.* [2006] used particle transport simulations to show that the neutron emission off a planetary surface was not isotropic but had a polar angle dependence that deviated from isotropy by $\sqrt{\cos\theta_s}$, where θ_s is the polar emission angle from the normal to the surface. We tested the *Maurice et al.* [2004] suggestion that the empirically determined value of η is due to anisotropic emission by substituting the LP-NS angular response into the neutron simulation, including the $\sqrt{\cos\theta_s}$ factor, and calculating neutron count rates for the same altitude range as that used by *Maurice et al.* [2004]. We find η_{sim} = 75º, which is close to the measured lunar value of 80º. In addition, when we replace the $\sqrt{\cos\theta_s}$ factor in the simulation with unity, we find η = 90º. We therefore conclude that the simulated neutron counts quantitatively agree with the suggestion of *Maurice et al.* [2004] that the measured anisotropy is due to an angular anisotropy of neutron emission from the planetary surface.

For the MESSENGER NS, the situation is complicated by the fact that the BP angular response is substantially more anisotropic than was the case for the boom-mounted LP-

NS. Specifically, the BP sensor response is similar to that of the LG sensors with a large efficiency for angles with a clear view to Mercury's surface and low efficiency in directions for which the view to Mercury is blocked by the spacecraft. Figure 12 shows simulated fast neutron counts versus altitude and isotropic solid angle (Equation 3).

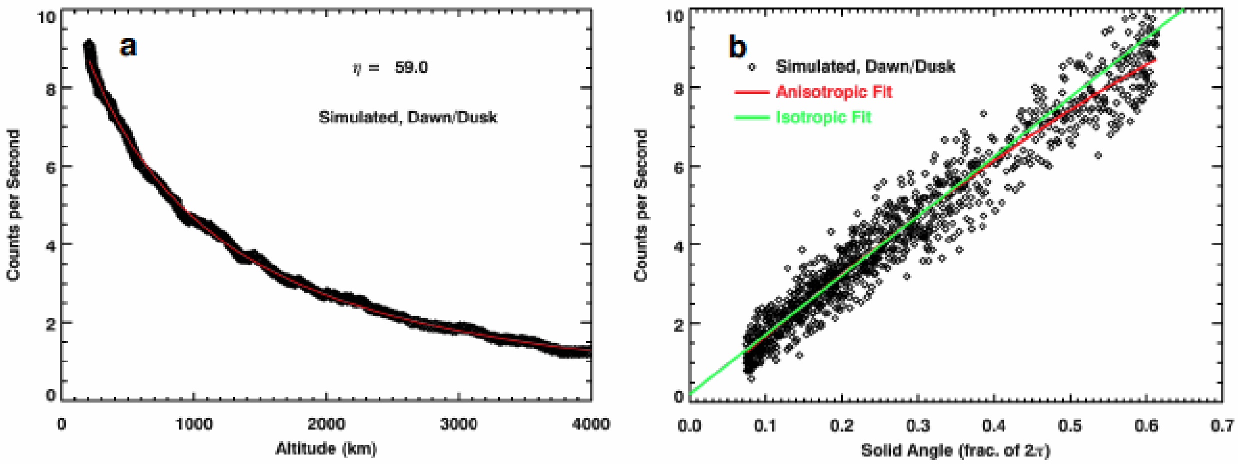

Figure 12. **(a)** Simulated fast neutron count rate versus altitude for dawn–dusk orbits. Poisson uncertainties have been applied to the simulation and data have been smoothed in altitude. An anisotropic solid angle (red) has been fit to the counts. **(b)** Unsmoothed, simulated fast neutron counts versus an isotropic solid angle function. Fit of an isotropic solid angle function (Equation S2) is shown as the green line; the fit of the anisotropic solid angle (Equation S3) is shown as the red line.

Actual spacecraft orbital parameters were used for the simulation and restricted to specific dawn–dusk orbits during which the spacecraft was constantly nadir pointing. This orientation was chosen to ensure that the only count rate variation not related to surface composition was due to solid angle. For this set of simulated counts, we included Poisson uncertainties to simulate the degree to which anisotropic solid angle effects can be quantified within this limited dawn–dusk dataset. The counts versus altitude (Figure 12a) were smoothed in altitude to reduce the scatter and provide more fidelity to an empirical fit to Equation 4. The plotted counts versus solid angle (Figure 12b) were not smoothed. Figure 12a shows a fit of Equation 4 to the simulated data (red line) where the best-fit η value is $\eta = 59^{o}$. An alternate view of the data is shown in Figure 12b where both the isotropic and anisotropic fits are shown. The effect of the anisotropic solid angle is to reduce the relative counts near the planet, which results from the fact that at lower altitudes Mercury fills a larger FOV for the detector and begins to be obscured by detector-surrounding spacecraft components. To test the sensitivity of the η value obtained from the fit when using Poisson uncertainties, 1000 separate simulation cases with different random number seeds were run and η values were fit for each case. Figure 13 shows that the mean η value is 60° with a one-standard deviation uncertainty of 4°.

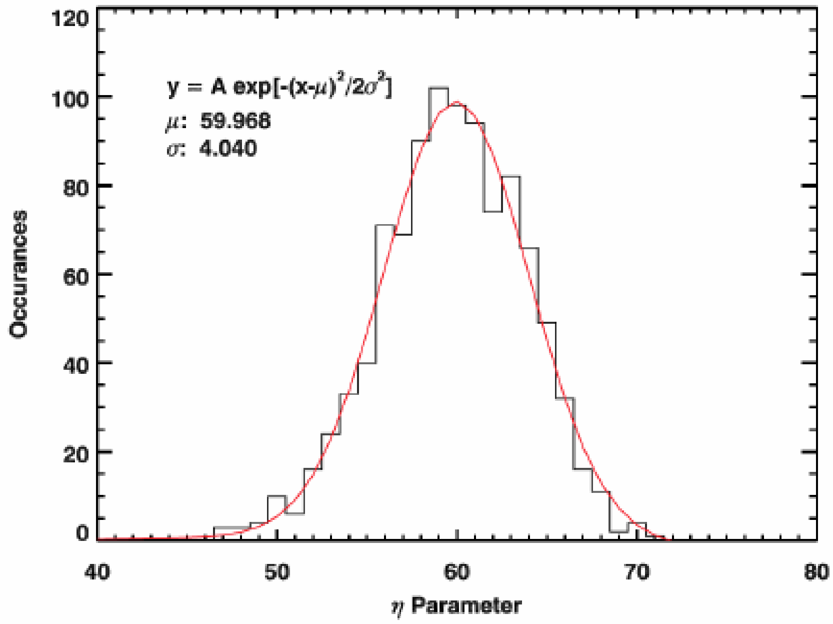

Figure 13. Histogram of fit values of η for 1000 separate runs of simulated dawn–dusk fast neutron counts with Poisson statistics included.

Measured fast neutron data for the identical orbit selection as was used for the simulations in Figure 12 are shown in Figure 14. Here, an offset of 1.547 cps was subtracted from the net fast neutrons and the counts were included to an altitude of 10,000 km. The fit η value of η_{meas} = 59.3° is nearly identical to the simulated value. This result provides an additional validation of the simulated neutron counts. A plausible interpretation of the η = 60° value derived for MESSENGER compared with the η_{LP} = 80° value for LP is that for the MESSENGER measurements there is a substantial anisotropy in the detection and emission, whereas for the LP measurements only the neutron emission contains a significant anisotropy.

As a final check, we investigated the dependence of η on spacecraft orientation, namely nadir angle. As illustrated in Figure 15, nadir angle is defined as the angle between the spacecraft z-axis and the spacecraft-to-planet-center vector (or local nadir).

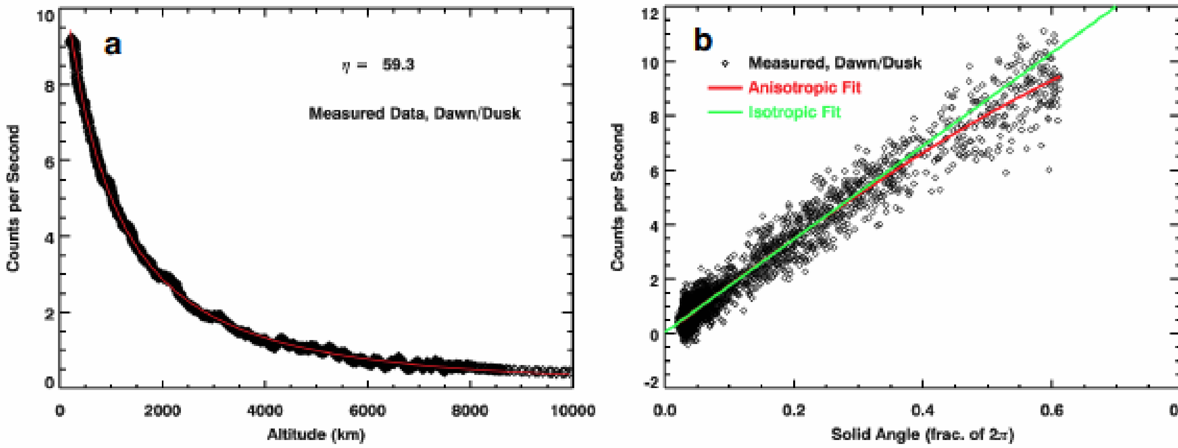

Figure 14. **(a)** Measured fast neutron count rate versus altitude for dawn–dusk orbits. Data have been smoothed in altitude. An anisotropic solid angle (red) has been fit to the counts. **(b)** Unsmoothed, measured fast neutron counts versus an isotropic solid-angle function. Fit of an isotropic solid angle function is shown as the green line; the fit of the anisotropic solid angle is shown as the red line.

As defined here, for positive nadir angles, the NS has a clear view to the planet; for negative nadir angles, the spacecraft blocks the NS view to the planet.

For the same orbital parameters as in Figure 12, simulated fast neutron counts were calculated, but with nadir angles varying from -40° to +40° (this range of nadir angles was not encountered during the actual mission but can be calculated with the simulation to provide a range of fit η values). The results of this set of simulations are shown in Figure 16. Figure 16a shows the fit to count rate dependence versus isotropic solid angle for each nadir angle. Figure 16b shows the fit η value versus nadir angle. As seen, there is a small variation of η for negative nadir angles and a minimum at a nadir angle of 0° (note: the data of Figures 12–14 were determined with a nadir angle of 0°). For positive nadir angles, there is a relatively large variation that approaches η = 90°. The average nadir angle for the selected data results in an effective η value of η = 66°. As will be shown, this approximation is validated by the combined analysis of simulated and measured data.

4.3.2. Radial Doppler Effect

The anisotropic emission and detection effects on solid angle apply equally to epithermal neutrons and to fast neutrons. However, epithermal neutrons have an additional effect that must be quantitatively understood to better than 1%: the radial Doppler effect. As

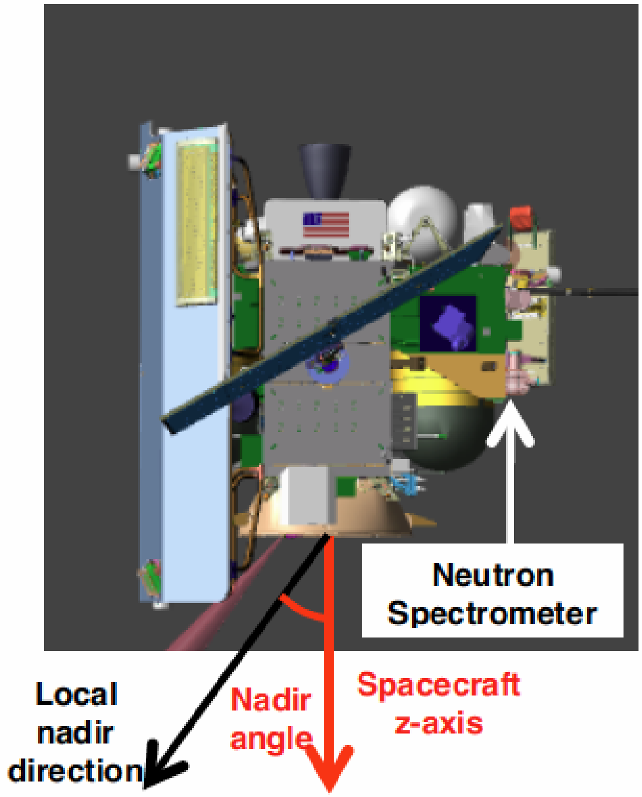

Figure 15. View of the MESSENGER spacecraft looking toward the positive x-axis. The z-axis points down, and an example local nadir direction is shown. The NS is located on the right side of the figure. Nadir angle is defined as the angular difference between the spacecraft z-axis and the direction of local nadir.

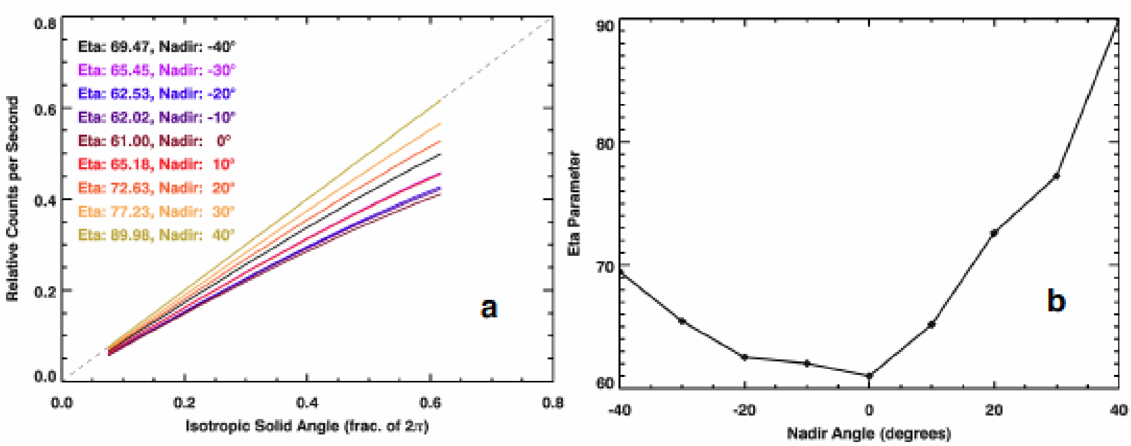

Figure 16. **(a)** Simulated fast neutron counts for nominal dawn–dusk orientation but with variable spacecraft nadir angle. **(b)** Fit values of η versus nadir angle for simulated fast neutron data.

was originally presented by *Feldman and Drake* [1986], a neutron Doppler effect occurs when the speed of a low-energy neutron (typically ~2 km/s) is comparable with the speed of the orbiting spacecraft around a planet. When this condition holds, observable enhancements or decreases of neutron counts depend on the orientation of the neutron sensor to the spacecraft velocity vector. The Doppler effect has become a standard technique for separating thermal from epithermal neutrons for planetary neutron spectroscopy [e.g., *Maurice et al.*, 2011]. For prior studies, the neutron measurements were made from a polar orbiting spacecraft with a near-constant altitude so that the along-track velocity component was responsible for the full Doppler effect. In contrast, the highly eccentric MESSENGER orbit has substantial velocity components with respect to Mercury in both the along-track and radial directions. Specifically, the MESSENGER along-track velocity ranges from <1 to 3.5 km/s, and the radial velocity ranges from -1.5 km/s to +1.5 km/s, where a positive velocity indicates an incoming direction and a negative velocity indicates an outgoing direction. As a consequence, low-energy neutrons measured by the MESSENGER NS will manifest a radial Doppler effect that causes a relative increase for incoming portions of the orbit and a relative decrease for outgoing portions of the orbit. The radial Doppler effect will go to zero around periapsis at locations where the radial velocity component is zero. Although this effect will be most pronounced for thermal neutrons, prior measurements have shown that the low-energy portion of the epithermal neutrons can have a detectable Doppler effect [*Maurice et al.*, 2004].

To illustrate the radial Doppler effect, simulated epithermal neutron count rates were calculated for the same set of dawn–dusk orbits that formed the basis for the simulation for fast neutrons in Section 3.3.1. Because of the orientations selected, the only variations in the data unrelated to surface composition should be from variations in solid angle. Figure 17 shows the simulated epithermal neutron count rates versus altitude separated into incoming (black) and outgoing (red) portions of the orbits. As seen, the count rates from the incoming portions are systematically higher than for the outgoing portions. This shift disappears at periapsis. The phase and magnitude (a few percent) of the shift are consistent with that of a radial Doppler effect.

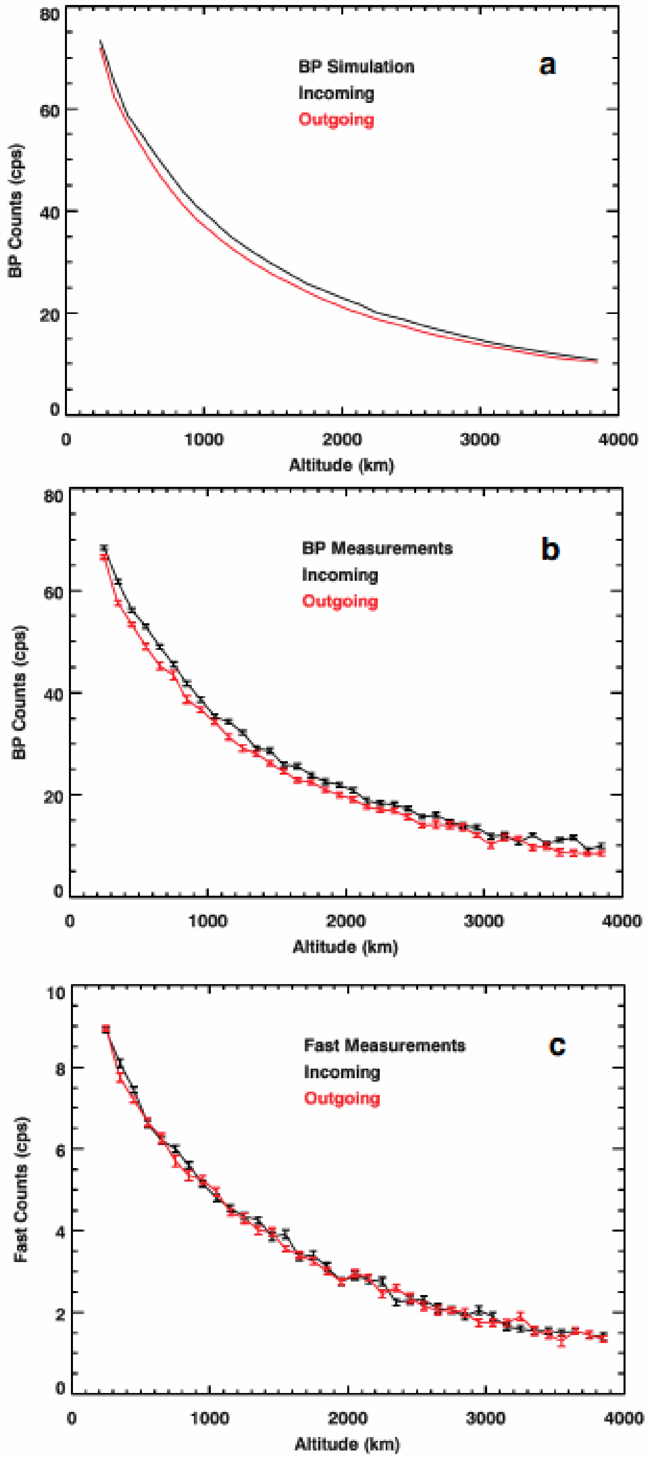

Figure 17. (a) Simulated epithermal (BP) neutron counts for a dawn–dusk orbits separated into incoming (black) and outgoing (red) portions of the orbits. **(b)** Measured epithermal neutron counts for dawn–dusk orbits separated into incoming and outgoing portions of the orbits. **(c)** Measured fast neutron counts for dawn–dusk orbits separated into incoming and outgoing portions of the orbits.

Measured epithermal neutron data for identical orbital parameters are shown in Figure 17b. The error bars denote the measured standard deviation for each altitude bin. The same shift between incoming and outgoing portions of the orbits seen in the simulated data is evident in the measured data. As a final check, Figure 17c shows fast neutron data for the same orbital parameters. Because of their large velocities relative to spacecraft velocities, fast neutrons should not show a vertical Doppler effect; this expectation is demonstrated by the lack of a shift between incoming and outgoing portions of the orbits. This full, quantitative agreement of simulation and data for the radial Doppler effect further validates the reliability of the neutron simulation for epithermal neutrons. A correction for a vertical Doppler effect for slow neutrons (thermal plus epithermal) measured with the GRS ACS was implemented by *Peplowski et al.* [2015]

4.3.3. Validation of Neutron Simulation: Summary

On the basis of the presented information, we consider the neutron simulation to be validated to a high degree of accuracy. To summarize, the neutron simulation code was initially validated with Mercury flyby data from the NS LG sensors along with absolute LP-NS count rates and count-rate variations [*Lawrence et al.*, 2010]. The discussion here, which was originally presented by *Lawrence et al.* [2013], has shown a high degree of correlation between simulated and measured fast and epithermal neutron count rates for a full range of spacecraft observational parameters. We have shown that the simulation agrees quantitatively with measurements of neutron emission and detection anisotropy. We have shown that the simulated epithermal neutron count rates predict measurements of a radial Doppler effect. Finally, *Peplowski et al.* [2015], *Peplowski et al.* [2016], and *Lawrence et al.* [2016a] have provided additional validations for the GRS ACS neutron, NS thermal neutron, and NS fast neutron measurements, respectively. This robust validation therefore provides strong confidence that the simulated neutron counts can be used to analyze the measured fast and epithermal neutron data in making measurements of neutrons from Mercury's surface to better than 1% accuracy.

5. Correction of Simulated and Measured Data

5.1. Principle of Analysis

A key part of the NS analysis is to compare the simulated and measured data, and through this comparison quantify signatures in the data that are due to variations in surface composition. A detailed comparison between simulated and measured data is required because the magnitudes of the compositional signatures are small compared with the systematic variations introduced to the neutron measurements by other effects. These systematic variations must be fully quantified and understood in order to isolate surface compositional variations.

The comparison of simulation and data must be carried out so as to avoid introducing new systematic variations not associated with variations in surface composition. Specifically, whereas the simulation explicitly accounts for all the three-dimensional neutron transport attenuation and transport effects through the spacecraft, it is unlikely that the absolute magnitudes of these effects are accurately and quantitatively simulated to the required level of better than 1%. Thus, a direct comparison of absolute, uncorrected simulated and measured data would result in systematic variations related to slight, quantitative inaccuracies in the neutron transport parameters.

To circumvent this difficulty, we did not directly compare uncorrected simulated counts with uncorrected measured counts. Rather, we used the simulated data as a guide to develop empirical data corrections for both the simulated and measured data. As stated previously, the simulated data were calculated for the same time stamps as the measured data. For different studies, the simulated data were calculated for different soil types, which has a non-hydrogen elemental composition [*Lawrence et al.*, 2016a] constrained by MESSENGER XRS and GRS data. For any specific comparison, the simulated counts were calculated for a single soil type, so that all count rate variations in the simulated data are by necessity the result of sensor response and spacecraft orientation effects. The precise elemental composition is of secondary importance, because a change in elemental concentrations of non-hydrogen elements results only in a scale-factor change in simulated neutron count rates. Because the analysis of neutron observations uses relative neutron count rate variations, such a scale-factor change does not affect the relative count rates. The assumed spatial uniformity of the elemental concentrations is a separate and potentially more important issue. From the GRS ACS and fast neutron data we find that there is small compositional variability across the mapped surface, especially compared with fast neutron measurements on other planetary bodies [*Peplowski et al.*, 2015, *Lawrence et al.*, 2016a].

With the full simulated dataset, we implemented data correction algorithms that force the "corrected simulated data" to have a flat or well-defined variation in count rate across the surface. The extent to which the final count rate spatial distribution is flat (fast neutrons) or well defined (epithermal neutrons) demonstrates the validity of the derived empirical corrections. One added benefit of the data simulation is that statistical uncertainties can be turned on and off. When turned off, subtle effects that might be largely masked by the statistical variations can be clearly delineated in the simulated data.

The empirical algorithms derived from the simulated data were applied to the measured data. Differences in neutron transport parameters that are difficult to quantify were captured with empirical correction parameters. After all data were fully corrected for non-composition variations, the simulated and measured data were compared and surface compositional effects investigated.

5.2. Summary of Corrections and Selections

When the above procedure was implemented, a number of corrections and selections were applied to the data. Some corrections were applied only to the simulated data, some were common to both datasets, and some were applied only to the measurements. All data selection criteria, for example removal of time periods due compromised data quality, were applied equally to both simulated and measured data. The sections below describe all the implemented corrections and selections.

5.3. Simulation-only Corrections

The one correction that was applied only to the simulated data was a scaling factor that was described in Section 3.2. The offset factor described in Section 3.2 was applied to the data.

5.4. Data Selections

A number of data selections were carried out to optimize the final analyzable dataset. The first set of selections involved eliminating time periods when the sensor background was unacceptably large or the NS parameter configuration was not set for nominal data collection. Solar energetic particle (SEP) events create large backgrounds in the NS that complicate fitting the spectral continuum and reduce the signal-to-background of the neutron peak. As a consequence, times of SEP activity (Table 1) were eliminated from the NS dataset [see also *Lawrence et al.*, 2016b]. Magnetospheric energetic electron (EE) events [*Lawrence et al.*, 2015a] also result in enhanced backgrounds in the BP sensor and were likewise removed from the dataset, using the procedure outlined in Section 4.6.4.

Finally, there were a number of times during spacecraft orbit-correction maneuvers (OCMs) when the NS high voltage (HV) was lowered for sensor safety reasons, but the NS continued with nominal data collection. Data from these times (Table 2) were also eliminated from the final dataset.

A second set of selections was applied to the data in order to optimize the NS viewing geometry. There are three viewing geometry selections of altitude, nadir angle, and *x*-axis angle. For the study of *Lawrence et al.* [2013] the altitude selection required the final dataset to have altitudes less than 1500 km. This selection provides optimum coverage for all northern latitude regions where the altitude is always less than 1500 km and limits the inclusion of less statistically significant higher-altitude data than observations taken at lower altitudes. The nadir-angle selection requires the final dataset to have nadir angles between -45º and +45º. This selection provides for a maximal amount of collected data while restricting wide nadir angles that require the largest correction factors. The final selection was for the *x*-axis angle, which is defined as the angle between the spacecraft *x*-axis (i.e., the solar panel rotation axis) and the spacecraft-to-planet vector. During most data collection, the *x*-axis angle was very close to 90º. To simplify the data correction procedure, we restricted the *x*-axis angle to ±3º of 90º. The benefit of the *x*-axis selection is that NS response variations are constrained to two dimensions (rotations around the *y*- and *z*-axis), thus eliminating an additional source of systematic variations unrelated to composition. Other studies used different types of selections [*Peplowski et al.*, 2015, 2016, *Lawrence et al.*, 2016a].

SEP	Day start	Time start	Day stop	Time stop	SEP	Day start	Time start	Day stop	Time Stop
1	3/24/11	11:48:19	3/24/11	18:50:03	57	4/24/13	21:13:05	4/26/13	12:00:00
2	3/25/11	5:52:23	3/25/11	10:15:36	58	4/27/13	21:43:47	4/28/13	2:06:58
3	3/25/11	23:01:18	3/26/11	4:28:38	59	4/28/13	12:10:43	4/28/13	14:59:34
4	3/30/11	17:00:00	3/30/11	22:00:00	60	5/10/13	18:34:28	5/11/13	2:00:00
5	4/4/11	9:48:40	4/4/11	13:56:56	61	5/13/13	15:30:16	5/14/13	13:37:42
6	5/24/11	22:00:00	6/3/11	3:45:00	62	5/15/13	3:28:50	5/15/13	5:16:17
7	6/4/11	6:13:13	6/15/11	22:00:00	63	5/31/13	19:40:00	6/1/13	2:37:40
8	8/2/11	5:39:24	8/2/11	18:24:21	64	6/21/13	3:08:22	6/25/13	2:00:00
9	8/4/11	3:33:28	8/5/11	17:00:00	65	8/19/13	22:29:50	8/22/13	22:00:00
10	8/9/11	7:00:00	8/10/11	3:00:00	66	10/5/13	6:27:55	10/7/13	22:00:00
11	9/5/11	5:39:00	9/8/11	14:00:00	67	10/11/13	6:33:02	10/16/13	5:16:17
12	9/6/11	4:45:00	9/6/11	7:10:00	68	10/20/13	6:02:20	10/20/13	13:01:53
13	9/7/11	4:01:00	9/7/11	6:32:00	69	10/22/13	20:32:00	10/23/13	20:37:16
14	9/7/11	18:58:00	9/8/11	6:00:00	70	10/25/13	7:29:00	10/27/13	12:00:00
15	9/8/11	22:20:00	9/10/11	2:00:00	71	10/28/13	4:09:00	10/31/13	12:00:00
16	9/22/11	11:25:40	9/24/11	8:00:00	72	11/2/13	4:35:00	11/3/13	6:00:00
17	10/4/11	12:53:49	10/6/11	2:55:42	73	11/4/13	5:46:00	11/5/13	4:25:00
18	10/14/11	12:56:57	10/15/11	10:13:16	74	11/5/13	21:43:00	11/5/13	23:01:00
19	10/17/11	8:10:30	10/17/11	11:38:16	75	11/7/13	10:48:00	11/9/13	22:00:00
20	11/3/11	22:50:16	11/6/11	2:00:00	76	11/19/13	9:57:00	11/21/13	12:00:00
21	11/9/11	12:56:40	11/9/11	18:45:00	77	11/29/13	3:59:00	11/29/13	20:07:00
22	11/17/11	20:52:37	11/18/11	16:50:00	78	11/30/13	2:37:00	12/2/13	3:23:00
23	12/14/11	14:20:00	12/14/11	22:30:00	79	12/5/13	11:34:00	12/5/13	20:53:00
24	12/25/11	17:48:00	12/26/11	15:55:00	80	12/13/13	20:06:00	12/15/13	12:00:00
25	1/2/12	14:54:00	1/3/12	13:50:00	81	12/26/13	3:13:00	12/31/13	22:00:00
26	1/23/12	5:36:00	2/6/12	0:01:00	82	1/6/14	7:19:05	1/11/14	22:00:00
27	3/3/12	20:11:00	3/17/12	0:00:00	83	1/22/14	3:59:32	1/23/14	7:00:00
28	4/5/12	21:13:05	4/6/12	0:14:30	84	1/27/14	22:00:00	1/31/14	5:52:00
29	4/9/12	11:04:13	4/9/12	17:17:43	85	2/11/14	3:03:15	2/11/14	21:02:00
30	4/26/12	8:25:36	4/26/12	12:10:43	86	2/12/14	6:07:27	2/12/14	12:10:00
31	4/27/12	16:00:00	4/28/12	2:58:00	87	2/14/14	15:45:00	2/15/14	12:32:00
32	5/17/12	2:32:33	5/19/12	2:37:40	88	2/18/14	0:29:45	2/19/14	4:00:00
33	5/26/12	20:16:48	5/30/12	2:42:00	89	2/20/14	7:00:00	2/21/14	6:00:00
34	6/28/12	16:04:00	6/29/12	17:00:00	90	2/25/14	3:44:11	3/5/14	6:00:00
35	7/1/12	18:58:00	7/2/12	2:00:00	91	3/14/14	21:28:00	3/14/14	12:00:00
36	7/2/12	10:18:10	7/2/12	18:09:00	92	3/29/14	16:41:00	3/30/14	7:00:00
37	7/3/12	3:03:15	7/3/12	11:04:13	93	4/29/14	19:09:00	4/29/14	23:00:00
38	7/12/12	16:26:11	7/14/12	19:30:00	94	5/5/14	14:44:00	5/5/14	20:48:00
39	7/17/12	17:00:00	7/21/12	2:00:00	95	6/4/14	19:24:00	6/5/14	7:00:00
40	7/23/12	3:52:00	7/29/12	12:00:00	96	6/10/14	11:19:00	6/10/14	14:20:00
41	7/30/12	18:34:28	7/30/12	21:59:08	97	6/12/14	21:38:00	6/13/14	15:14:00
42	7/31/12	21:47:30	8/1/12	3:00:00	98	7/11/14	12:56:46	7/11/14	13:58:10
43	9/8/12	11:14:27	9/8/12	17:33:04	99	8/8/14	12:05:36	8/9/14	12:00:00
44	9/19/12	10:48:00	9/25/12	2:00:00	100	8/24/14	11:45:00	8/24/14	21:00:00
45	9/28/12	9:50:00	10/1/12	2:00:00	101	9/1/14	8:35:00	9/7/14	7:10:00
46	10/8/12	12:22:25	10/9/12	9:52:50	102	9/8/14	20:00:00	9/9/14	7:49:47
47	10/14/12	0:30:30	10/14/12	20:27:11	103	9/10/14	16:41:00	9/13/14	0:45:00
48	10/23/12	2:57:19	10/23/12	3:27:48	104	9/25/14	0:55:00	9/28/14	9:57:00
49	10/26/12	11:29:47	10/26/12	19:51:10	105	10/15/14	14:49:00	10/17/14	1:36:00
50	11/8/12	1:45:18	11/8/12	9:47:18	106	11/3/14	9:11:00	11/5/14	17:53:00

51	11/18/12	3:33:20	11/18/12	10:06:41	107	12/13/14	10:59:00	12/23/14	0:29:00
52	11/21/12	13:42:49	11/22/12	3:54:25	108	12/26/14	9:15:00	12/27/14	2:00:00
53	2/5/13	8:10:15	2/5/13	11:09:20	109	2/21/15	9:32:00	2/23/15	2:32:33
54	3/15/13	17:58:39	3/17/13	4:40:28	110	3/24/15	8:20:29	3/28/15	15:40:30
55	4/11/13	5:52:06	4/13/13	2:12:05	111	4/5/15	4:25:07	4/5/15	16:16:19
56	4/21/13	6:33:02	4/23/13	2:00:00	112	4/14/15	0:24:38	4/16/15	0:24:38

Table 1. Start and stop times for Solar Energetic Particle (SEP) events during the MESSENGER Mercury orbital mission.

Maneuver	Day start	Time start	Day stop	Time stop	Maneuver type
1	5/9/11	19:22:00	5/9/11	22:55:00	300 second data
2	6/15/11	16:00:00	6/15/11	21:39:00	HV to zero for s/c thrust
3	7/26/11	17:33:59	7/26/11	21:58:24	HV to zero for s/c thrust
4	9/7/11	11:30:00	9/7/11	16:15:00	HV to zero for s/c thrust
5	10/24/11	18:29:00	10/24/11	23:16:00	HV to zero for s/c thrust
6	12/5/11	12:36:00	12/5/11	17:18:00	HV to zero for s/c thrust
7	3/2/12	22:09:22	3/3/12	2:47:54	HV to zero for s/c thrust
8	4/16/12	17:17:00	4/21/12	1:20:55	HV to zero for 8-hour orbit
9	11/26/12	18:03:00	11/29/12	18:30:00	BP elect. gain change
10	6/17/14	12:10:00	6/17/14	16:01:00	HV to zero for low-altitude s/c thrust
11	9/12/14	13:01:00	9/12/14	17:07:00	HV for low-altitude s/c thrust
12	9/28/14	7:44:40	9/28/14	8:25:36	HV to zero for EE safe mode
13	10/24/14	16:11:12	10/24/14	20:06:34	HV for low-altitude s/c thrust
14	1/21/15	15:35:00	1/21/15	19:35:52	HV for low-altitude s/c thrust

Table 2. Start and stop times for spacecraft maneuvers during the MESSENGER Mercury orbital mission.

5.5. Common Simulation/Measurement Corrections

A number of corrections were carried out that were common to both the simulated and measured datasets. These are corrections for solid angle, sensor/spacecraft response, and radial Doppler effect. Each of these corrections is described below.

5.5.1 Solid Angle Corrections: Epithermal Neutrons

As described in Section 3.3, we used an anisotropic solid angle given by Equations 4 and 5 to characterize the solid angle and determined that a value of η = 66º best characterizes the weighting of the nadir angles from -45º to +45º. When the counts versus solid angle are plotted for the full range of nadir angles, an additional nadir angle dependence was found such that the slope of the function describing counts versus solid angle (e.g., Figure 12b) was dependent on nadir angle. Figure 18 shows how this slope varies with nadir angle for both the simulated and measured data. A similar set of nadir angle versus offset parameters was also calculated. The slope parameters of Figure 18

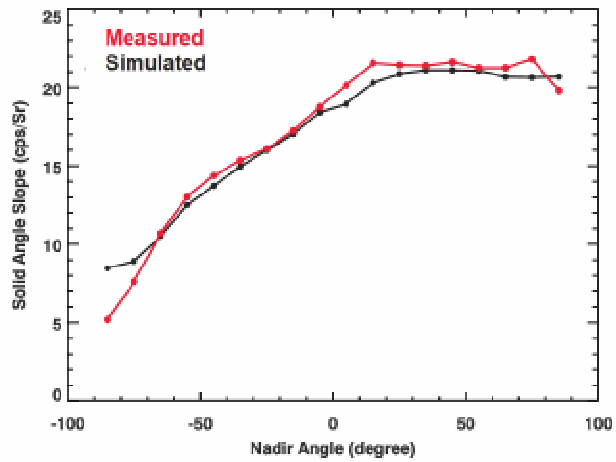

Figure 18. Correction factors for solid angle slope (counts versus solid angle) for simulated (black) and measured (red) data using data selections described in the text.

were derived for a separate set of data selections: altitude < 3000 km, 87º < *x*-axis angle < 93º, and latitude < 45ºN. This latitude selection was implemented to ensure that no effects of polar compositional variations in the measured data could affect the data correction factors. Figure 18 shows that for the final nadir angle selections of -45º to +45º, the simulated and measured slope values are similar in shape and magnitude. The simulated and measured offset values are also in good agreement. This result both provides a further validation of the simulation and justifies the range -45º to +45º for nadir angle selection. The least accurate agreement between simulated and measured data occurs for nadir angles less than -45º and reflects the maximum amount of neutron transport through spacecraft material and hence conditions for which the simulation is least likely to be an accurate estimate of the actual spacecraft response.

The solid angle correction for the simulated and measured data was carried out in the following manner. For each measurement time step, an interpolated solid angle slope and offset were determined from the measured solid angle and the values of Figure 18. The data were then corrected using the following algorithm:

$$C_1 = C_0 - f_{SA}\left(\theta_{NA},\Omega\right) + f_{SA}\left(\theta_{SA},\Omega_{400}\right) , \quad (6)$$

where C_0 and C_1 are the initial and corrected counts, respectively. θ_{NA} and Ω are the nadir angle and solid angle, respectively; $f_{SA}(\theta_{NA},\Omega) = a(\theta_{NA})\Omega + b(\theta_{NA})$ is the solid angle

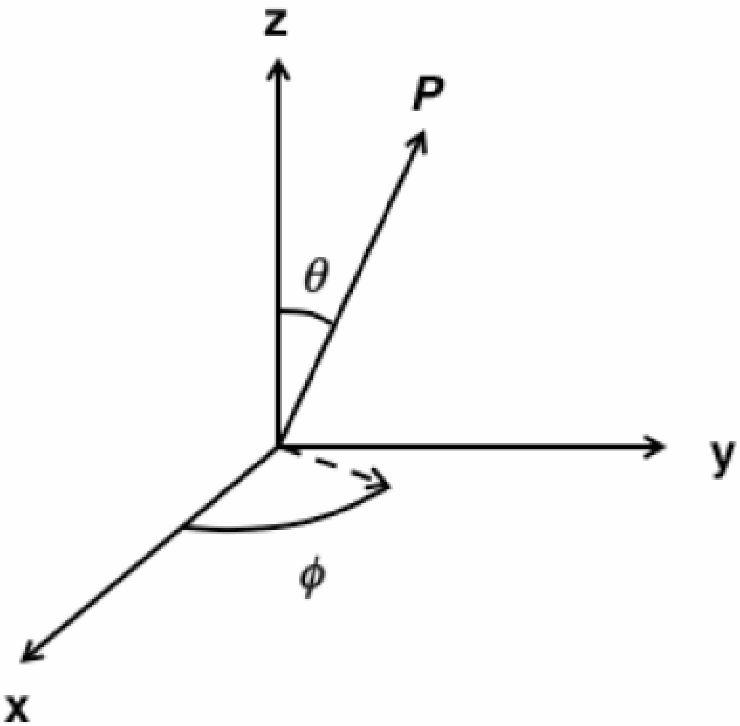

Figure 19. Rotational coordinate system defined for the angular spacecraft obscuration corrections. Axes are the MESSENGER spacecraft axes, and the vector ***P*** is the spacecraft pointing direction to the Mercury subsurface point. The rotational angle ϕ is defined so that negative angles are pointing through the spacecraft and positive angles provide an unobstructed view of the NS to the Mercury surface.

correction function where $a(\theta_{NA})$ and $b(\theta_{NA})$ are the nadir-angle-dependent slope (e.g., Figure 18) and offset parameters. The last term of Equation 6 corrects the data to a common altitude of 400 km, for which the solid angle is Ω_{400}.

5.5.2 Spacecraft Obscuration Corrections: Epithermal Neutrons

The neutron detection response of the NS varies markedly as a function of arrival angle into the NS (see Section 4.1.2). To correct for this viewing geometry variation, we used both the simulated and measured data to derive an empirical correction response. With the spherical coordinate system defined in Figure 19, the mean counts were calculated for θ and ϕ bins for both the simulated and measured data. A two-dimensional correction was used because the angular response is not separable into individual θ or ϕ correction factors. To avoid any bias in this correction due to possible latitude-dependent compositional variations, only data equatorward of 45° were used to derive the correction factor. Also note that the data for each (ϕ, θ) bin cover multiple spatial locations on

Mercury's surface so that biases from any non-polar compositional variations will be muted.

Example two-dimensional correction factors for the simulated and measured fast neutron data are shown in Figure 20. The simulated response map has no statistical uncertainties included. There is a strong agreement between the two response maps, which provides an additional validation of the simulation. In particular, for negative ϕ angles for which the NS is obstructed by the spacecraft, the response is small, and for positive ϕ angles for which the NS has a clear view to Mercury's surface, the response is large. Black areas indicate portions of the (ϕ, θ) phase space where no NS measurements were obtained.

The response function correction was carried out using the two-dimensional response map as a lookup table for each (ϕ, θ) measurement combination. The final selected data are a subset of the values shown in Figure 20 so that all final time step measurements have a valid response function correction factor. The count rate for each measurement time step was divided by the response function value to arrive at a time series dataset of relative count rates.

5.5.3. Solid Angle and Spacecraft Obscuration Corrections for Fast Neutrons

The fast neutron correction for variable instrument response due to different instrument look directions and spacecraft distances to Mercury's surface was carried out as described in *Lawrence et al.* [2016a]. Following *Peplowski et al.* [2015] a two-dimensional correction was implemented to simultaneously account for variations in response with nadir angle and spacecraft distance. The spacecraft distance was parameterized by the fractional solid angle, Ω, subtended by Mercury in the omnidirectional NS. The measured and modeled two-dimensional response is shown in Figure 21. That the measured and modeled values are virtually identical provides confidence that the modeled values are properly accounting for the non-GCR count-rate variations. The two-dimensional response correction was accomplished by assigning each fast-neutron measurement a correction factor $R(\Omega,\theta_{NA})$, given in units of counts per second (cps) on the basis of the values in Figure 21. The fast-neutron count rate was divided by this correction to obtain a relative fast-neutron count rate.

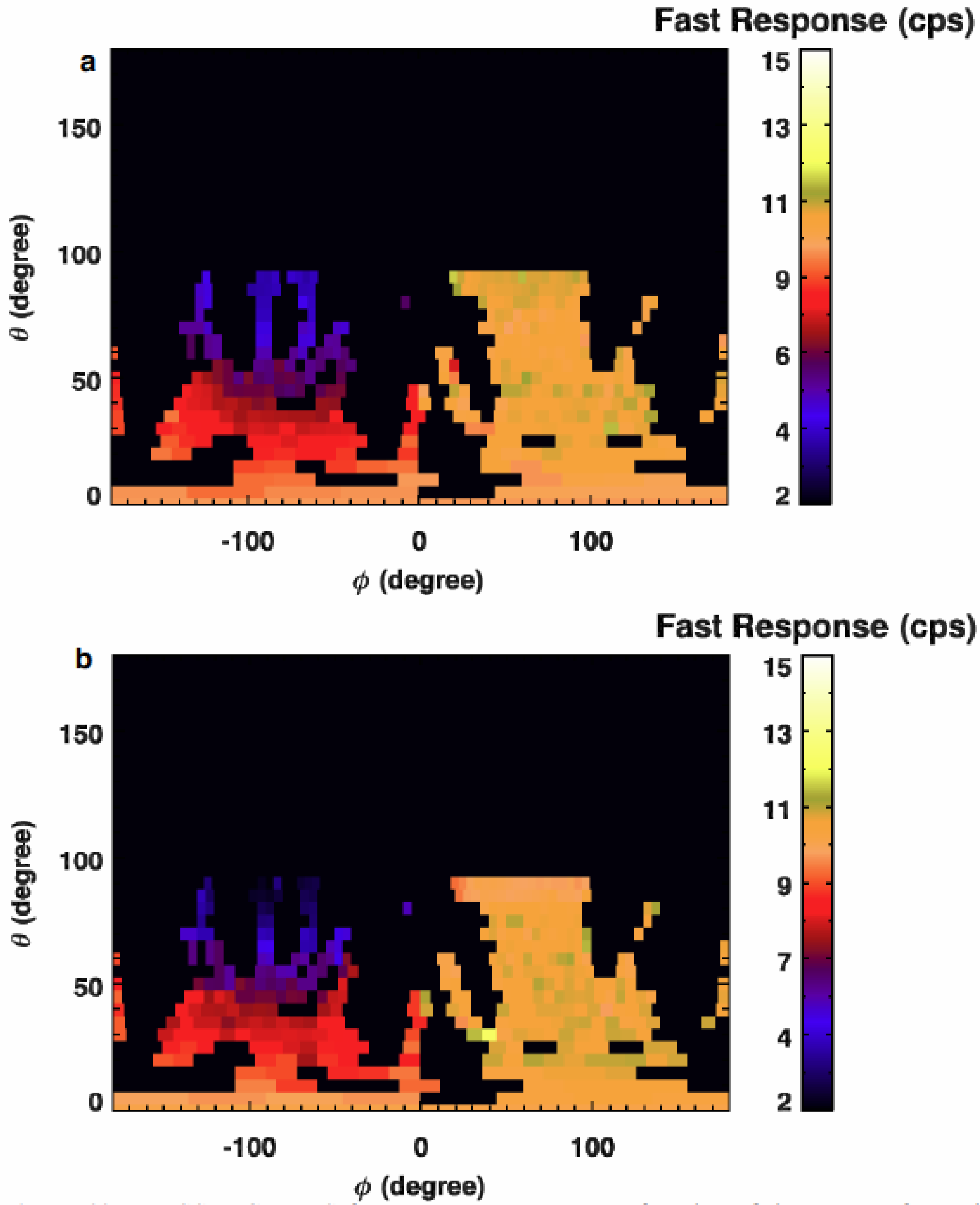

Figure 20. MESSENGER NS fast neutron response as a function of the spacecraft rotation angles θ and ϕ. (**a**) Simulated and (**b**) measured response. Count rate response is determined for altitudes less than 1500 km and latitudes less than 45ºN and is given in units of counts per second.

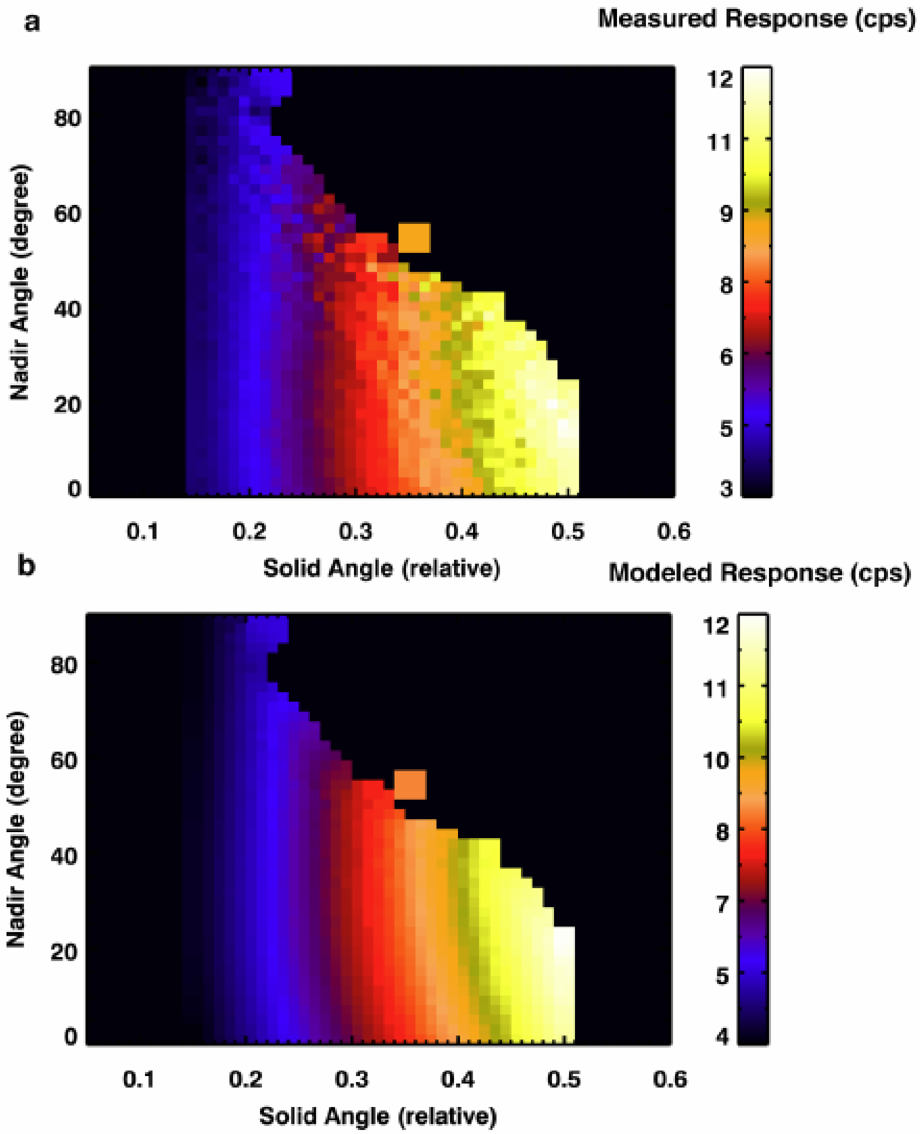

Figure 21. Solid angle (relative to a value of 1 at the surface of Mercury) versus nadir-angle response for (**a**) measured and (**b**) modeled count rates.

5.5.4. Vertical Doppler Correction

The correction for the vertical Doppler effect (see also Section 4.3.2) is the final correction that was carried out for both the simulated and measured data and applies only to epithermal neutrons. This correction was carried out in the manner described in the main text of *Lawrence et al.* [2013].

5.6. Corrections Only to Measurements

The final corrections are those that were applied only to the measured data. These include corrections for sensor gain, background counts, GCR variations, dead-time variations, EE events, and surface temperature effects. Each correction is described below.

5.6.1. BP Sensor Gain and Background Counts

The BP sensor gain correction is described in Section 2, and that for background counts is described in Section 3.2.

5.6.2. NS Dead Time

The NS event procesing time, τ, is approximately 25 μs, and the total NS event counter, C_E, ranges from 800 to 1100 events per second. Because the total event counter is small compared with the inverse of τ, the total NS dead time and its variation are therefore small. The NS dead-time fraction, τ_{frac}, was determined with a non-paralyzable approximation that is appropriate for small relative count rates:

$$\tau_{\mathrm{frac}} = \frac{1}{1 + C_E \tau} \quad (7).$$

A dead-time correction was made to each time stamp measurement in the time series data using the dead-time fraction value. For high-count rate measurements during solar particle events, additional dead-time corrections were carried out. A description of these corrections is given in Appendix A of *Lawrence et al.* [2014].

5.6.3 Galactic Cosmic Ray Variations

Planetary neutron fluxes vary in response to time variability of the planet-incident GCR flux. An independent measurement of the incident GCR flux therefore must be obtained in order to correct the neutron count rate for GCR variations. The NS has a triple coincidence mode in which any event that deposits energy in all three NS sensors is registered. For protons, energies greater than 120 MeV are required to produce a triple coincidence event [*Feldman et al.*, 2010], making the triple coincidence counter an ideal measure of the local GCR flux, which is the dominant source of high-energy protons. This triple-coincidence count rate has been found to be a good approximation to the GCR variations [*Lawrence et al.*, 2016b]. For each orbit, the mean triple-coincidence count rate was measured for altitudes greater than 8000 km. Only triple-coincidence data acquired far from the planet were used to avoid planet obscuration effects when near Mercury. These data were normalized to the triple-coincidence count rate measured early in the mission to arrive at a GCR proxy factor that is close to unity. A detailed description of how this proxy was derived is given by *Lawrence et al.* [2016b]. Figure 22 shows the triple-coincidence count rate for the full MESSENGER orbital mission. The GCR proxy is a normalized version of this count rate as described in *Lawrence et al.* [2016a]

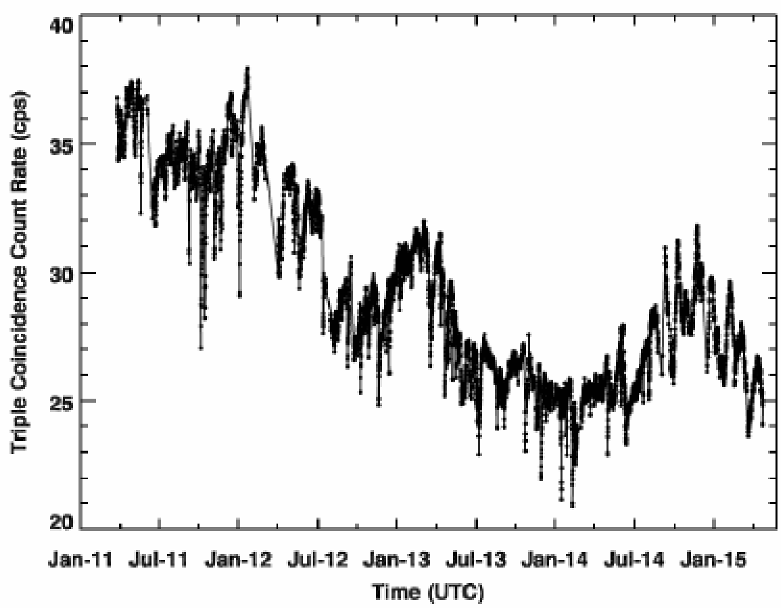

Figure 22. Time variation in the NS triple-coincidence count rate, which is used as a proxy for GCR variations.

5.6.4. Energetic Electron (EE) Event Variations

Lawrence et al. [2015a] characterized energetic electron (EE) events within Mercury's magnetosphere as measured with the MESSENGER NS and GRS ACS. Specifically, the NS BP sensor is highly sensitive to bremsstrahlung X-rays produced when energetic electrons hit spacecraft materials near the NS. This correction is primarily needed for the BP epithermal neutrons. EE events do not affect the fast neutron measurements, which are based on a double-coincidence pulse measurements. A brief description is given here regarding how EE events affect the BP epithermal neutron measurement.

Because the NS is highly sensitive to EE events, NS data are used to identify and characterize EE events. NS BP data from 3 May 2011, a day on which there were multiple EE events, are shown in Figure 23. Figure 23a shows derived net epithermal neutron counts for altitudes less than 4000 km versus a time index, defined as the successive accumulation period at altitude less than 4000 km starting at the beginning of the day. Each time index value is 20-s in length. Figure 23b shows a quantity termed EE signal-to-background (or EE signal) that measures the signal magnitude of EE events [*Lawrence et al.*, 2015a]. As seen in Figure 23, there were two large EE events that had a signal greater than 5 and lasted for greater than 10 min. For these two large events, the net neutron count rate clearly undershot the expected value. The reason for this difference is that the power-law background shape adopted in Section 2 is violated during the EE events, which have higher counts in the low-energy channels than at times when EE events are not present.

The derived net-count rate, shown in Figure 24, is linearly related to the EE signal size. Figure 25 further shows that the spatial locations of EE events are clustered around the latitude ranges -10° to 30°N and 40° to 60°N.

Because the large EE events cause systematic errors in the derived net neutron count rates, all time stamps with an EE event size greater than 5 were removed from the analysis dataset. As seen in Figure 23b and Figure 25, this selection removed the largest events that create the largest systematic error. A more strict selection would remove too much data and result in an unacceptable loss in statistical sampling.

From the empirical relation shown in Figure 24, EE event signals lower than 5 can result in systematic errors comparable in magnitude to the expected signal size from Mercury polar hydrogen signatures. Thus, the relation illustrated in Figure 24 was used to correct all the time-series data to reduce the magnitude of the EE event background. As seen in Fig. 3A of *Lawrence et al.* [2013], this empirical EE background correction does not entirely eliminate systematic variations with latitude that are consistent with the

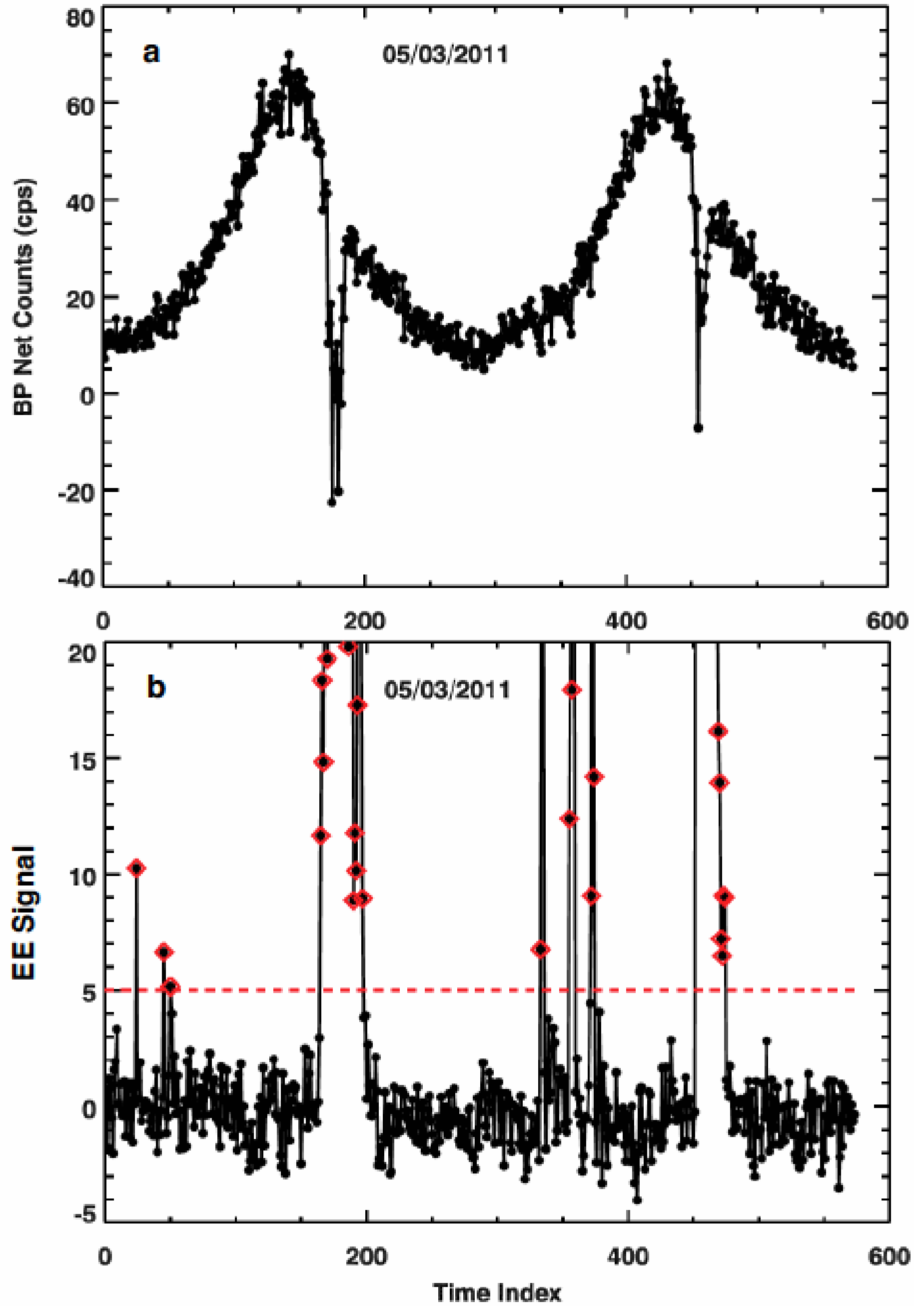

Figure 23. (a) Derived net epithermal neutron counts for two Mercury orbits from 3 May 2011 and altitudes less than 4000 km. Net counts are plotted versus the time index, the data collection index for all 20-s collection periods within the day. **(b)** Derived EE event signal to noise as a function of time index for the same time period as the data in (A).

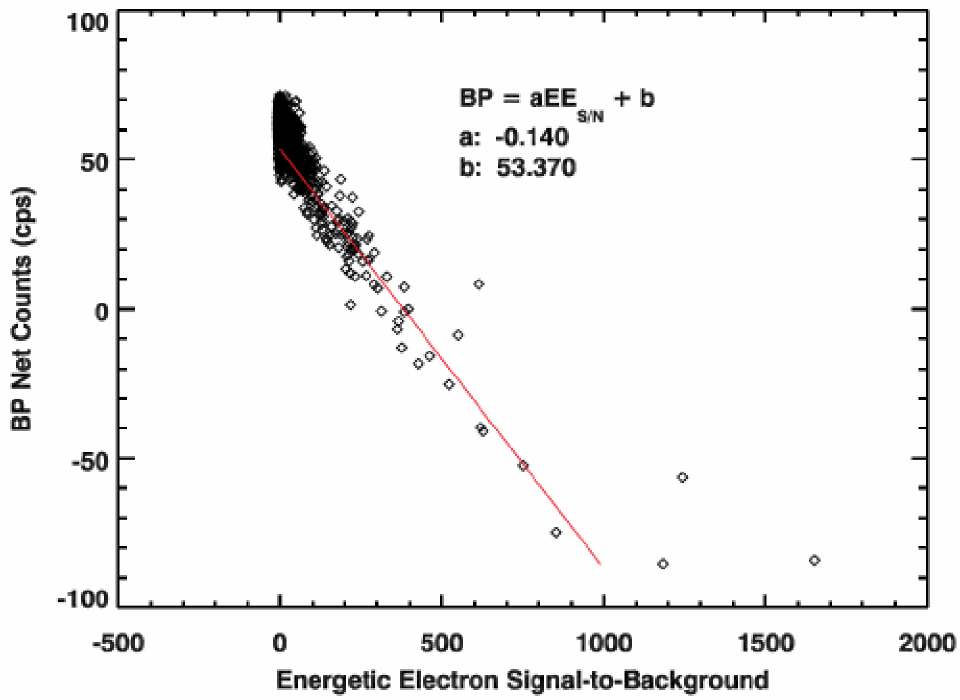

Figure 24. Derived net epithermal neutron counts versus EE event signal.

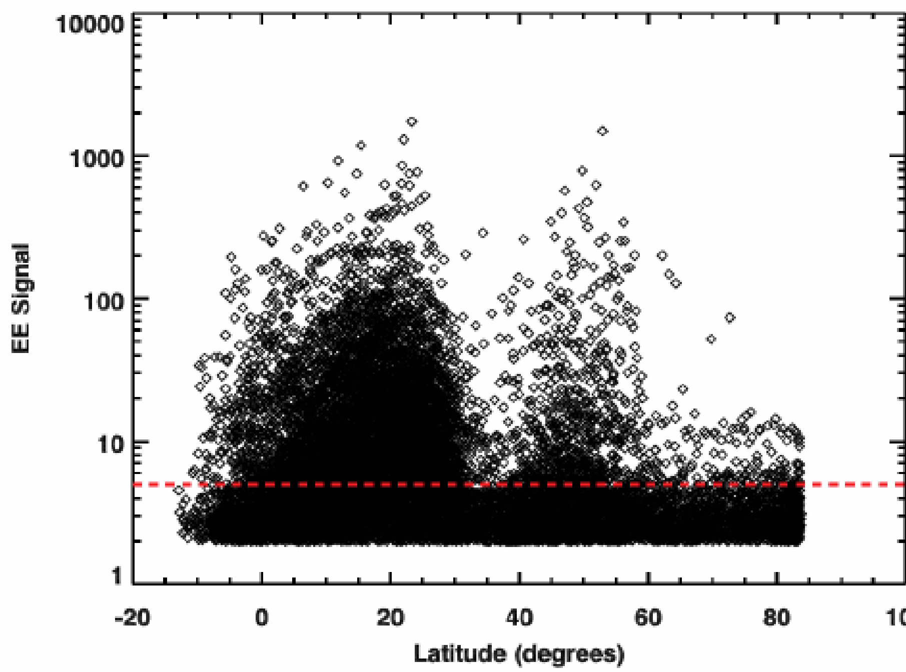

Figure 25. EE signal versus latitude for all identified EE events. The dashed red line is at an EE event size of 5.

EE events. This imperfect correction is likely due to the fact that the linear approximation of Figure 24 breaks down for small EE events. Indeed, ad hoc variations in the empirical EE background correction can further reduce the systematic, non-polar latitude biases from that shown in Fig. 3A of *Lawrence et al.* [2013]. However, given that the current systematic uncertainties are less than 0.5%, and that a more generalized and physics-based EE correction has yet to be derived, the current EE background correction is adequate given the other sources of measurement uncertainty.

References:

Feldman, W., et al. (2004), Gamma-Ray, Neutron, and Alpha-Particle Spectrometers for the Lunar Prospector mission, *Journal of Geophysical Research-Planets*, *109*(E7), doi:10.1029/2003JE002207.

Feldman, W. C., and D. M. Drake (1986), A Doppler Filter Technique To Measure The Hydrogen Content Of Planetary Surfaces, *Nuclear Instruments & Methods in Physics Research Section a-Accelerators Spectrometers Detectors and Associated Equipment*, *245*(1), 182-190, doi:10.1016/0168-9002(86)90274-3.

Feldman, W. C., D. M. Drake, R. D. O'Dell, F. W. Brinkley, and R. C. Anderson (1989), Gravitational effects on planetary neutron flux spectra, *J Geophys Res*, *94*(B1), 513-513, doi:10.1029/JB094iB01p00513.

Feldman, W. C., et al. (2010), Evidence for extended acceleration of solar flare ions from 1-8 MeV solar neutrons detected with the MESSENGER Neutron Spectrometer, *J. Geophys. Res. Space Physics*, *115*, doi:10.1029/2009JA014535.

Feldman, W. C., D. J. Lawrence, W. T. Vestrand, D. N. Baker, P. N. Peplowski, and D. J. Rodgers (2015), Long-duration neutron production by nonflaring transients in the solar corona, *J. Geophys. Res. Space Physics*, *120*(10), 8247-8266, doi:10.1002/2015JA021042.

Goldsten, J. O., et al. (2007), The MESSENGER Gamma-Ray and Neutron Spectrometer, *Space Sci. Rev.*, *131*(1-4), 339-391, doi:10.1007/s11214-007-9262-7.

Ho, G. C., et al. (2011), MESSENGER Observations of Transient Bursts of Energetic Electrons in Mercury's Magnetosphere, *Science*, *333*(6051), 1865-1868, doi:10.1126/science.1211141.

Lawrence, D. J., S. Maurice, and W. C. Feldman (2004), Gamma-ray measurements from Lunar Prospector: Time series data reduction for the Gamma-Ray Spectrometer, *J Geophys Res*, *109*(E7), E07S05-E07S05, doi:10.1029/2003JE002206.

Lawrence, D. J., W. C. Feldman, R. C. Elphic, J. J. Hagerty, S. Maurice, G. W. McKinney, and T. H. Prettyman (2006), Improved modeling of Lunar Prospector neutron spectrometer data: Implications for hydrogen deposits at the lunar poles, *J Geophys Res*, *111*(E8), E08001, doi:10.1029/2005JE002637.

Lawrence, D. J., W. C. Feldman, J. O. Goldsten, T. J. McCoy, D. T. Blewett, W. V. Boynton, L. G. Evans, L. R. Nittler, E. A. Rhodes, and S. C. Solomon (2010), Identification and measurement of neutron-absorbing elements on Mercury's surface, *Icarus*, *209*(1), 195-209, doi:10.1016/j.icarus.2010.04.005.

Lawrence, D. J., J. K. Harmon, W. C. Feldman, J. O. Goldsten, D. A. Paige, P. N. Peplowski, E. A. Rhodes, C. M. Selby, and S. C. Solomon (2011), Predictions of MESSENGER Neutron Spectrometer measurements for Mercury's north polar region, *Planet Space Sci*, *59*(13), 1665-1669, doi:10.1016/j.pss.2011.07.001.

Lawrence, D. J., et al. (2013), Evidence for water ice near Mercury's north pole from MESSENGER Neutron Spectrometer measurements, *Science*, *339*(6117), 292-296, doi:10.1126/science.1229953.

Lawrence, D. J., W. C. Feldman, J. O. Goldsten, P. N. Peplowski, D. J. Rodgers, and S. C. Solomon (2014), Detection and characterization of 0.5-8 MeV neutrons near Mercury: Evidence for a solar origin, *J. Geophys. Res. Space Physics*, *119*(7), 5150-5171, doi:10.1002/2013JA019037.

Lawrence, D. J., et al. (2015a), Comprehensive survey of energetic electron events in Mercury's magnetosphere with data from the MESSENGER Gamma-Ray and Neutron

Spectrometer, *J. Geophys. Res. Space Physics*, *120*(4), 2851-2876, doi:10.1002/2014JA020792.

Lawrence, D. J., W. C. Feldman, P. N. Peplowski, and S. C. Solomon (2015b), The 4 June 2011 neutron event at Mercury: A defense of the solar origin hypothesis, *J. Geophys. Res. Space Physics*, *120*(7), 5284-5289, doi:10.1002/2015JA021069.

Lawrence, D. J., P. N. Peplowski, A. W. Beck, W. C. Feldman, E. A. Frank, T. J. McCoy, L. R. Nittler, and S. C. Solomon (2016a), Compositional Terranes on Mercury: Information from Fast Neutrons, *Icarus*, doi:10.1016/j.icarus/2016/07.018.

Lawrence, D. J., P. N. Peplowski, W. C. Feldman, N. A. Schwadron, and H. E. Spence (2016b), Galactic cosmic ray variations in the inner heliosphere from solar distances less than 0.5AU: Measurements from the MESSENGER Neutron Spectrometer, *J. Geophys. Res. Space Physics*, *121*, doi:10.1002/2016JA022962.

Leary, J. C., et al. (2007), The MESSENGER Spacecraft, *Space Sci. Rev.*, *131*(1-4), 187-217, doi:10.1007/s11214-007-9269-0.

Masarik, J., and R. C. Reedy (1996), Gamma ray production and transport in Mars, *Journal of Geophysical Research-Planets*, *101*(E8), 18891-18912, doi:10.1029/96je01563.

Maurice, S., D. J. Lawrence, W. C. Feldman, R. C. Elphic, and O. Gasnault (2004), Reduction of neutron data from Lunar Prospector, *J Geophys Res*, *109*(E7), E07S04, doi:10.1029/2003JE002208.

Maurice, S., W. Feldman, B. Diez, O. Gasnault, D. J. Lawrence, A. Pathare, and T. Prettyman (2011), Mars Odyssey neutron data: 1. Data processing and models of water-equivalent-hydrogen distribution, *J Geophys Res*, *116*(E11), E11008-E11008, doi:10.1029/2011JE003810.

McKinney, G., D. Lawrence, T. Prettyman, R. Elphic, W. Feldman, and J. Hagerty (2006), MCNPX benchmark for cosmic ray interactions with the Moon, *Journal of Geophysical Research-Planets*, *111*(E6), doi:10.1029/2005JE002551.

Pelowitz, D. B. (2005), MCNPX User's Manual, Version 2.5.0*Rep.*, 473-473 pp, Los Alamos, New Mex.

Peplowski, P. N., D. J. Lawrence, W. C. Feldman, J. O. Goldsten, D. Bazell, L. G. Evans, J. W. Head, L. R. Nittler, S. C. Solomon, and S. Z. Weider (2015), Geochemical terranes of Mercury's northern hemisphere as revealed by MESSENGER neutron measurements, *Icarus*, *253*, 346-363, doi:10.1016/j.icarus.2015.02.002.

Peplowski, P. N., R. L. Klima, D. J. Lawrence, C. M. Ernst, B. W. Denevi, E. A. Frank, J. O. Goldsten, S. L. Murchie, L. R. Nittler, and S. C. Solomon (2016), Remote sensing evidence for an ancient carbon-bearing crust on Mercury, *Nature Geoscience*, *9*(4), 273-276, doi:10.1038/ngeo2669.

Prettyman, T. H., et al. (2011), Dawn's Gamma Ray and Neutron Detector, *Space Sci. Rev.*, *163*(1-4), 371-459, doi:10.1007/s11214-011-9862-0.

Rodgers, D. J., D. J. Lawrence, W. C. Feldman, and P. N. Peplowski (2015), Neutrons and energetic charged particles in the inner heliosphere: Measurements of the MESSENGER Neutron Spectrometer from 0.3 to 0.85 AU, *J. Geophys. Res. Space Physics*, *120*(2), 841-854, doi:10.1002/2014JA020263.